Sensitivity Studies for CTA to detect the *Fermi* Bubbles at low latitudes

Master's Thesis in Physics

Presented by
Dominic Bernreuther
May 25, 2018

Erlangen Centre for Astroparticle Physics
Friedrich-Alexander-Universität Erlangen-Nürnberg

Supervisor: **Prof. Dr. Stefan Funk**
Co-advisor: **Dr. Dmitry Malyshev**

Abstract

The *Fermi* Bubbles (FB) are one of the most spectacular features in the gamma-ray sky detected by the Fermi-LAT, but their origin is still unclear. With the Cherenkov Telescope Array (CTA) it will be possible to study the base of the *Fermi* Bubbles in an unprecedented resolution and learn about their origin. In this work an analysis strategy is developed to detect the *Fermi* Bubbles at low latitudes in the CTA data challenge. For this purpose the extended source sensitivity is estimated for CTA. According to this estimation, CTA will be sensitive to the *Fermi* Bubbles for observation times larger than 50 h. The analysis takes advantage of the tentative asymmetry with respect to the Galactic Center (GC) of the southern low-latitude *Fermi* Bubbles and its harder spectrum. Using the Spectral Component Analysis (SCA), the *Fermi* Bubbles can be filtered out from most of the background sources. The SCA component correlated with a hard spectrum is similar to what one expects from the *Fermi* Bubbles. A template is derived by applying two cuts on the signal in the hard component to verify that the signal comes most likely from the *Fermi* Bubbles.

Contents

1 Motivation

The *Fermi* Bubbles were originally revealed by the Fermi Large Area Telescope (LAT), as a possible gamma-ray counterpart of the microwave haze (Dobler et al. 2010; Finkbeiner 2004). These large-scale structures in the gamma-ray sky extend 50° ($\sim 10\,\mathrm{kpc}$) above and below the Galactic Center (GC) and have a width of about 40° in longitude (Su et al. 2010). In addition, these structures have sharp edges (Ackermann, Albert, et al. 2014). An illustration of the *Fermi* Bubbles is shown in figure 1. The spatial uniform spectrum of the *Fermi* Bubbles can be described by a power law and an exponential cut-off or a significant softening around 110 GeV (Ackermann, Albert, et al. 2014). Furthermore, there is no significant variation of the gamma-ray intensity within the *Fermi* Bubbles at high latitudes.

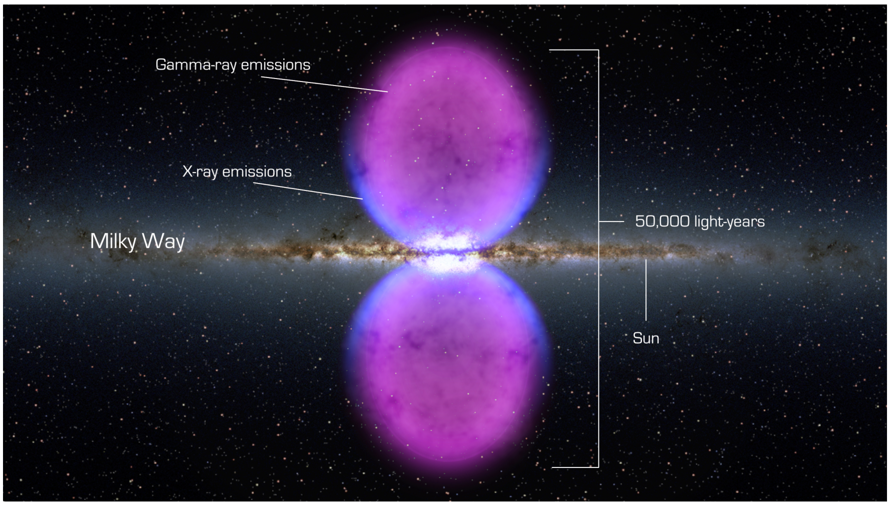

Figure 1: This artistic impression of the *Fermi* Bubbles shows the extending structures above and below the GC. The gamma rays observed by the Fermi Gamma-Ray Space Telescope are shown in magenta while the edges of the *Fermi* Bubbles, first observed in X-rays by ROSAT, are illustrated in blue. Figure taken from NASA April, 2018.

The low-latitude *Fermi* Bubbles, i.e., $|b| < 10°$, are of special interest, because of two main scenarios of their origin. While a starburst event or a stellar wind scenario would lead to a broad base of the *Fermi* Bubbles, which is not necessarily consistent with the GC, a scenario of an active past of the super massive black hole (SMBH) Sgr A* would lead to a narrow base of the *Fermi* Bubbles. Therefore, it would be interesting to investigate the *Fermi* Bubbles at low latitudes. The gamma-ray production mechanisms which are responsible for the gamma-ray emission of the low-latitude *Fermi* Bubbles are either leptonic or hadronic. In the leptonic scenario inverse Compton (IC) scattering produces the photons. In Compton scattering the high energy photons are scattered by low energy electrons. In this case the energy of the photons always decrease. However, if low energy photons are scattered by high energy electrons instead, then the photon energy increases. This effect is therefore called inverse Compton scattering (De Angelis et al. 2015). For instance, photons of the interstellar radiation field (ISRF) can be scattered by high energy electrons to very high energies. The ISRF consist mainly of the cosmic microwave background (CMB), infrared radiation from dust and starlight. The source of the high energy electrons are astrophysical accelerators like supernovae (SN) or active galactic nuclei (AGN). These two examples of accelerators will become interesting again if one talks about different theories of the origin and formation of the *Fermi* Bubbles (see chapter 3). In the hadronic scenario the high energy photons are generated by the decay of neutral pions (π^0). For example, the π^0 can be created in collisions of hadronic cosmic rays (CR) with gas where the π^0 decays immediately into two photons (Grupen 2005)

$$\pi^0 \longrightarrow \gamma + \gamma. \tag{1}$$

At low latitudes the *Fermi* Bubbles are brighter and the spectrum seems to be harder compared to higher latitudes (Ackermann, Ajello, et al. 2017). Consequently, one can expect gamma-ray emission above 100 GeV. Additionally, the Fermi-LAT data reveals an asymmetry of the southern low-latitude *Fermi* Bubbles with respect to the GC (Ackermann, Albert, et al. 2014). The analysis, developed in chapter 5, takes advantage of the harder spectrum and the asymmetry of the southern low-latitude *Fermi* Bubbles to separate the *Fermi* Bubbles from most of the other gamma-ray sources present in the GC. The most challenging part of the *Fermi* Bubbles analysis at low latitudes is to separate the *Fermi* Bubbles from other bright gamma-ray sources. Furthermore, it is not clear if the GC excess, discussed in Ackermann, Ajello, et al. 2017, has the same origin as the *Fermi* Bubbles.

Future instruments like the Cherenkov Telescope Array (CTA) can help to study the *Fermi* Bubbles at energies where the *Fermi*-LAT is not sensitive. CTA should be able to detect the *Fermi* Bubbles above 1 TeV. That means, CTA will possibly prove the assumption of a harder spectrum at low latitudes. Moreover, CTA has several improvements compared to current Cherenkov telescopes (see chapter 2), like sensitivity or a large field of view (FOV). Thus, CTA is a promising instrument to observe the *Fermi* Bubbles in the future.

In the following CTA data of the GC is simulated. The simulations are done with *ctools* and the model definitions of the first CTA data challenge (see chapter 4). The data is used to develop and present the analysis chain.

2 The Cherenkov Telescope Array

The Cherenkov Telescope Array (CTA) is a future ground based gamma-ray telescope to observe the universe at high energies. CTA will be built on two sites and therefore will consist of two arrays composed of so called Imaging Atmospheric Cherenkov Telescopes (IACT). One array will be placed in Chile referred to as the CTA-South, nearby the Cerro Paranal. The second array will be located on La Palma, Spain, which is referred to as the CTA-North. In this chapter the concept, main characteristics and some science goals of CTA are presented. Furthermore, this chapter deals with the idea to observe the *Fermi* Bubbles with CTA.

2.1 Introducing the CTA Science

CTA will help to get a better understanding of the very high energy universe[1] (VHEU) and will hopefully answer fundamental questions in astroparticle physics and beyond. As a major experiment in astrophysics, CTA will work together with gravitational wave and neutrino observatories as well as classical photon observatories to take part in multiple-messenger and multi-wavelength observations. This synergy is essential to solve astrophysical questions. There are three main topics CTA will cover which are listed in CTA Consortium et al. 2017.

The first goal is to understand the origin and the role of relativistic cosmic particles. These relativistic particles appear in many astrophysical systems like pulsars, supernova remnants (SNR), AGNs and galaxy clusters. The physical process of how these particles become highly relativistic is still under debate. Therefore, CTA will study the sites and mechanisms for particle acceleration in the universe. Particles are accelerated to very high energies in extreme environments, e.g., in the vicinity of neutron stars (NS) and black holes (BH). Hence, particle acceleration is associated with extreme environments, relativistic jets and massive explosions. CTA will observe extreme environments to understand the prevailing physical processes.

The last topic of CTA science deals with new frontiers in physics like Dark Matter (DM) and its distribution or quantum gravitational effects.

2.2 Principle of Detecting Gamma-Rays

There are two possible ways to detect gamma rays coming from astrophysical accelerators like SNRs or AGNs, to mention only two examples of astrophysical accelerators.

Satellites, orbiting the Earth, like the Fermi Gamma-Ray Space Telescope are designed to detect gamma-ray photons directly. Ground based telescopes like the CTA cannot detect directly, because the Earth's atmosphere shields life on earth from gamma rays. Therefore, gamma-ray photons cannot reach the ground. But CTA will use the atmosphere as a detector.

A primary photon, i.e., a single photon coming from the astrophysical source, enters the Earth's atmosphere and interacts with a nucleus about 10 km above

---

[1] referring to CTA Consortium et al. 2017 energies above 20 GeV

the ground producing a so called electromagnetic cascade (figure 2). Electromagnetic cascades consist of electron-positron pairs interacting with the electromagnetic field of a nucleus. These charged particles are producing secondary photons via Bremsstrahlung. As long as these secondary photons have enough energy to produce an electron-positron pair this is an ongoing process. Electrons and positrons, which propagate faster than the speed of light in air, emit Cherenkov light (Čerenkov 1937). This Cherenkov light is emitted in a cone-like shape and therefore Cherenkov photons are spread over a relatively large area on the ground, the so called light pool (figure 2). Single telescopes placed within this light pool can detect these Cherenkov photons with special designed cameras. These cameras can image the cascade by collecting as much Cherenkov photons as possible. In figure 2 an image of a single camera is shown. The amount of photons placed within a camera pixel is color coded. Due to an observation of the event, induced by the primary photon, with several telescopes the direction and energy of the primary photon can be reproduced.

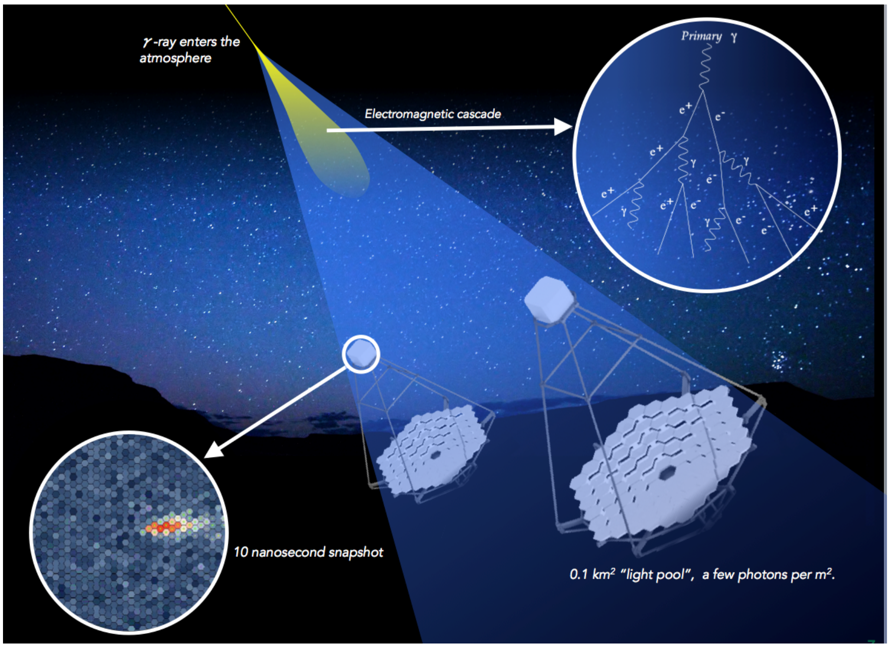

Figure 2: Artistic impression of the detection principle of CTA. An incoming primary photon interacts within the atmosphere producing an electromagnetic cascade. The resulting Cherenkov light is detected by several cameras which are installed on each telescope placed within the light pool. The direction and energy of the primary photon can be reconstructed by the elliptical shape of the detected photons. Figure taken from CTA March, 2018.

2.3 Characteristics and Perfomance

Due to several improvements, compared to currently existing instruments like H.E.S.S, MAGIC and VERITAS, CTA will be a promising experiment to tackle the astrophysical questions mentioned in section 2.1. Therefore, the characteristics of individual telescopes and of the whole telescope array will be discussed in this section.

The CTA will cover a wide energy range from 20 GeV to at least 300 TeV (CTA Consortium et al. 2017). Low energies provide access to the entire universe and are used to study extragalactic objects. High energies are needed to study extreme environments but can only be observed in the local universe like our own galaxy. This is because of the photon-photon absorption on the extragalactic background light. In addition, a wide energy range increases the probability to observe new sources of unknown spectral characteristics like DM particles. Additionally, the large energy coverage of CTA will also lead to more detailed studies of known sources.

The wide energy range requires three different telescope sizes (figure 3). Each telescope is equipped with highly reflective mirrors, espacially in the wavelength regime of Cherenkov light ($300\,\text{nm} \leq \lambda \leq 600\,\text{nm}$), and cameras consisting of several photomultiplier (PM). This combination leads to a high quantum efficiency of each telescope in the future.

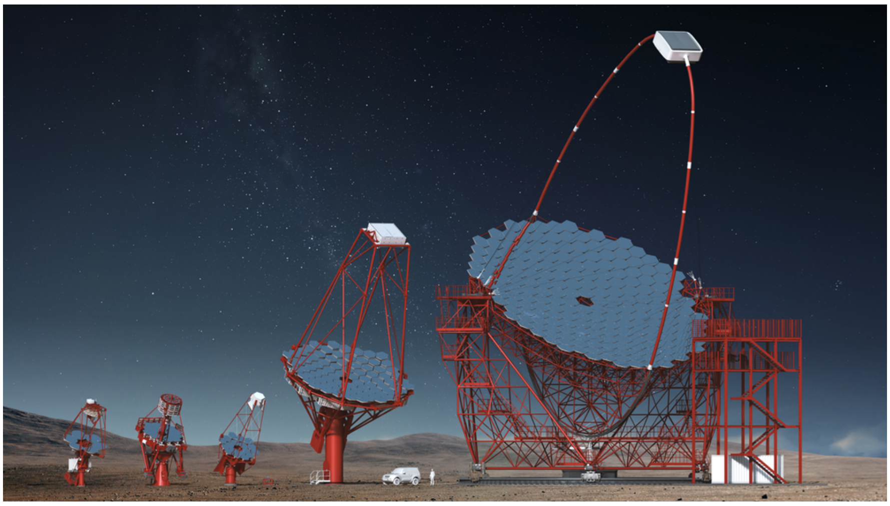

Figure 3: From the left: There are three SST prototype designs, which cover the highest energies. Each design works with a different technology. The MST covers the mid-range and the LST covers the lower part of the energy range. Figure taken from CTA March, 2018.

The Small-Sized Telescopes (SST) are responsible for the highest energies of the CTA, i.e., energies above 10 TeV (Mangano 2017). In fact, photons of these energies lead to much Cherenkov light but within a large light pool. Thus, CTA will consist of many SSTs, each with a mirror of only 4 m in diameter, spread over a large area on the ground (Mangano 2017). The Medium-Sized Telescopes (MST) cover the core energy range from 100 GeV to 10 TeV and have a diameter of about

12 m (Mangano 2017). In contrast to high energy photons, low energy photons with energies of about 20 GeV to a few hundred GeV produce a small amount of Cherenkov light. Hence, gathering Cherenkov photons from a low energy photon incident in the atmosphere requires telescopes with large mirrors. The Large-Sized Telescopes (LST) will have a mirror with a diameter of around 23 m (Mangano 2017) and will cover the low energy range of CTA.

To cover the full sky, CTA will be built on two sites. Each site has its own telescope configuration and is optimized for its science case. The CTA-South, on the southern hemisphere, will cover the whole energy range and will have access to the GC, which is a key target for the CTA. Therefore, CTA-South will be composed of four LSTs, 25 MSTs and 70 SSTs (Mangano 2017). The CTA-North, on the northern hemisphere, is optimized to observe the northern extragalactic sources and will only cover the low and the core energy range. This is because the GC is not visible on the northern hemisphere. Therefore, CTA-North will consist only of four LSTs and 15 MSTs (Mangano 2017). The two possible layouts of CTA-North and CTA-South can be seen in figure 4.

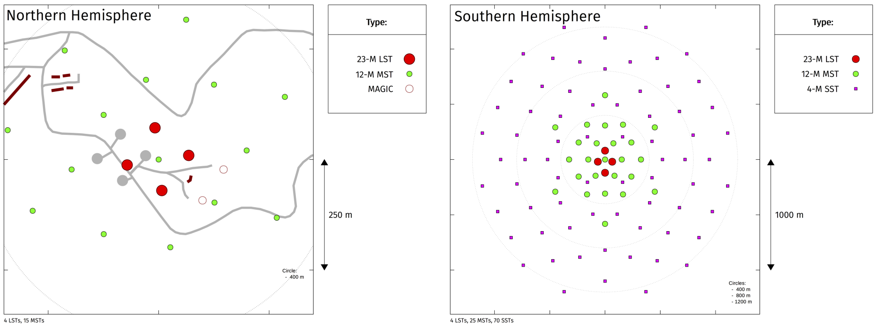

Figure 4: The possible layout of the two CTA sites. Different telescope types are color coded: (red) LSTs, (green) MSTs and (purple) SSTs. Left: Layout of the northern hemisphere array (CTA-North). Right: Layout of the southern hemisphere array (CTA-South). Figure taken from CTA March, 2018.

As shown in figure 1 the *Fermi* Bubbles are an extended gamma-ray source. To detect extended sources, CTA will have some special improvements. The camera of individual telescopes has a wide FOV starting from about 4.5° for the LST and 7° for the MST to larger than 8° for the SSTs (CTA Consortium et al. 2017). The large number of telescopes for each array and the wide FOV of individual telescopes provide a better collection of photons, even for large impact distances, resulting in an improved collection area and increase the FOV of the whole system. This characteristic of CTA is essential to observe extended objects and regions of diffuse gamma-ray emission like the *Fermi* Bubbles. Moreover, the wide FOV leads to a nearly uniform response to areas which are much larger than the spatial resolution of the array (CTA Consortium et al. 2017). The improved FOV compared to current instruments is one of the reasons why CTA should be able to detect the *Fermi* Bubbles.

CTA will also be able to image each event incident near the centre of the array multiple times (CTA Consortium et al. 2017). This image multiplicity is the reason for an improved background rejection which is in particular important to study extended and low-flux objects like the *Fermi* Bubbles. In combination with the large collection area, this leads to an improved point source sensitivity of CTA compared to current instruments (figure 5). The point source sensitivity of CTA peaks around a few TeV. This is the interesting energy range where CTA will be looking for the *Fermi* Bubbles. In addition, the image multiplicity provides also high energy and angular resolution. The angular resolution of CTA compared to other instruments is shown in figure 6. Above 100 GeV CTA has the best angular resolution of the gamma-ray instruments compared in this plot.

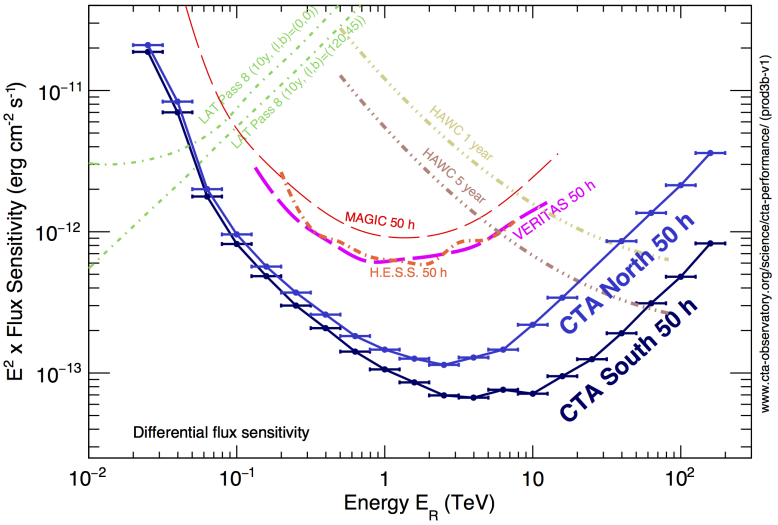

Figure 5: The differential sensitivity shown in this plot is defined as the minimum flux needed by CTA to obtain a 5σ detection of a point-like source. For comparison the sensitivity curves of current instruments are plotted together with the CTA sensitivity. Figure taken from CTA March, 2018.

One last feature of CTA which should be mentioned here is the ability to operate different sub-arrays with different pointing independently (CTA Consortium et al. 2017). This provides great flexibility for several observations. For example, groups of MSTs or SSTs may be used to monitor up to ten sources simultaneously or may be used to estimate the background (BKG) for an on-off like observation.

2.4 CTA and the Galactic Center

The Galactic Center is one key science project of CTA comprising a deep exposure of the inner few degrees of our galaxy. This region contains a great variety of high energy sources including the base of galactic outflows, currently known as *Fermi* Bubbles. The deep exposure and precise measurement with CTA will allow to study this particular region with unprecedented spatial and spectral detail and may lead to the disentangling of different models which try to explain extended emission like the *Fermi* Bubbles. CTA will follow different observation strategies to cover the whole key science project of the GC. One of them is referred to as

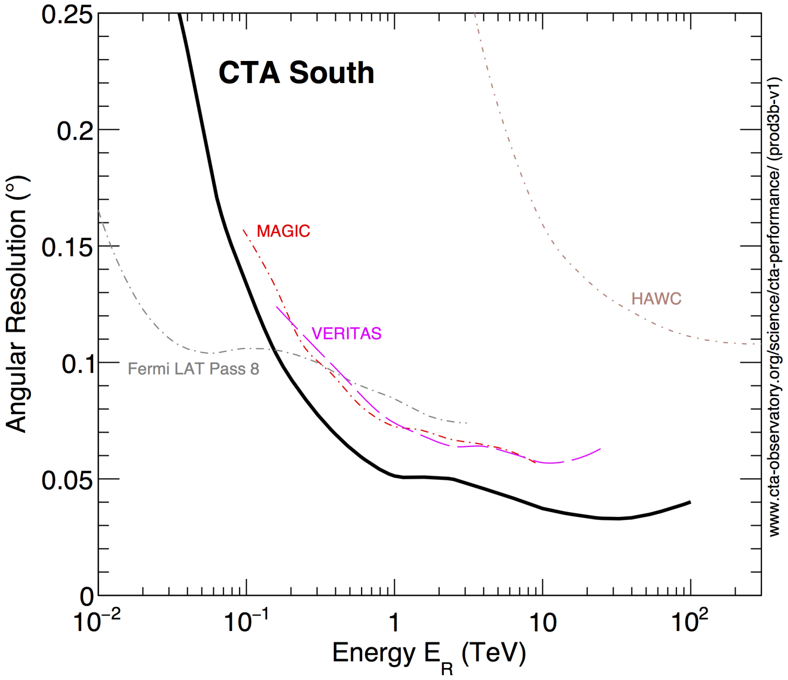

Figure 6: The angular resolution shows the angle within which 68% of reconstructed gamma rays are detected, relative to their true direction. Figure taken from CTA March, 2018.

the extended survey region with an exposure of around 300 h for the inner 10° in latitude (CTA Consortium et al. 2017). This exposure includes the base of the *Fermi* Bubbles which are subjects of the following chapters. The realization of this key science project is difficult because of the complexity of the GC. For instance, if one considers the *Fermi* Bubbles, which are larger than the FOV, CTA has still problems to model the corresponding background. Furthermore, the existing analysis focus on point sources rather than on extended sources like the *Fermi* Bubbles.

With the *Fermi* Bubbles in mind new analysis strategies have to be developed. This work is intended to develop an analysis to detect the *Fermi* Bubbles in the inner region of the GC, especially for negative latitudes. Therefore, the aim of this master's thesis is to contribute to the improvement of the extended source analysis.

3 *Fermi* Bubbles as a Gamma-Ray Source

The formation and the origin of the *Fermi* Bubbles are still open questions. Possible formation scenarios are an active past of the SMBH in the center of our galaxy or a nuclear starburst event. More details on these two scenarios are given below. The gamma-ray production within the *Fermi* Bubbles can be divided into a leptonic or hadronic scenario. Both are introduced in this chapter. The low-latitude *Fermi* Bubbles, i.e., within $|b| < 10°$, are the main focus of this work. Therefore, a separate subsection is devoted to this topic.

3.1 Gamma-Ray Production within the *Fermi* Bubbles

In this section the production of gamma-ray emission within the *Fermi* Bubbles is described. There are two possible emission mechanisms: The gamma-ray photons are produced by IC scattering of the ISRF with Cosmic Ray (CR) electrons and the interaction of high energy CR hadrons with the interstellar gas. The first one is referred to as the leptonic model and the latter one is referred to as the hadronic model.

3.1.1 Leptonic Model

In the leptonic, the *Fermi* Bubbles contain high-energy electrons that can upscatter ISRF photons by IC scattering. The observed gamma-ray spectrum can be explained by an electron population following a power law spectrum with an index $\gamma = 2.17$ and with an exponential cut-off energy $E_{\mathrm{cut}} = 1.25\,\mathrm{TeV}$ (Ackermann, Albert, et al. 2014). There is an overlap of the microwave haze and the gamma-ray *Fermi* Bubbles at latitudes $|b| < 35°$ (Ackermann, Albert, et al. 2014). Indeed, with a magnetic field in the range of 5 µG to 20 µG, the *Fermi* Bubbles can be produced by the same population of electrons like the microwave haze (Dobler et al. 2010; Su et al. 2010; Ackermann, Albert, et al. 2014). But as shown in Ackermann, Albert, et al. 2014 the main contribution of the IC emission of the *Fermi* Bubbles comes from electrons with energies above 100 GeV while the main contribution to the microwave haze comes from electrons between 10 GeV to 30 GeV. Thus, the signal could be explained by two distinct electron populations. However, there are some problems of the leptonic model. Producing photons of a few GeV out of the ISRF at a distance of 10 kpc requires electron energies of about 1 TeV. Taking only IC losses into account, the cooling time of these electrons is at most 1 Myr. If the electrons are produced near the GC, the transport velocity to high latitudes, where the *Fermi* Bubbles are still present, should be above $10^4\,\mathrm{km\,s^{-1}}$ (Ackermann, Albert, et al. 2014). This velocity is larger than the speed of sound in the plasma around the Galactic Plane (GP). Therefore, one would expect a shock front at the edge of the *Fermi* Bubbles, but no such shock front is observed until now (Malyshev 2017). Moreover, the gas outflow velocity observed from the GC is below $10^3\,\mathrm{km\,s^{-1}}$ (Fox et al. 2015). Consequently, the electrons have to be re-accelerated via the second Fermi acceleration mechanism (Mertsch et al. 2011; Cheng et al. 2011).

3.1.2 Hadronic Model

The hadronic model considers CR hadrons above 1 GeV interacting with the interstellar gas. If one follows the argumentation in Ackermann, Albert, et al. 2014 the main processes are proton-proton collisions. In these collisions, e.g., neutral pions are produced. The pions decay into two gamma-ray photons which can be detected. The spectrum of the high energy protons within the *Fermi* Bubbles has to be harder than the proton spectrum in the GP. In addition, the protons have to be trapped within the *Fermi* Bubbles for several Gyr to avoid that the protons escape before they interact with the interstellar gas, i.e., there must be a mechanism to keep the protons within the *Fermi* Bubbles.

Because of the pion cut-off around 100 MeV, there is a small deviation of the primary gamma-ray spectrum from the observed *Fermi* Bubbles spectrum. But the interaction of high energy protons also produces secondary leptons like electrons, positrons and neutrinos. The electrons and positrons emit gamma radiation due to IC and synchrotron losses. These losses can be used to compensate the deviation in the spectra (Ackermann, Albert, et al. 2014; Malyshev 2017). Unfortunately, these secondary leptons cannot explain the microwave haze. Thus, in the hadronic model an additional electron population or a re-acceleration of secondary leptons is needed to explain the microwave haze (Ackermann, Albert, et al. 2014). Neutrinos are only produced in the hadronic model. Therefore, a neutrino signal coming from the *Fermi* Bubbles would be an evidence for CR hadrons interacting with the interstellar gas and produce at least parts of the gamma-ray emission within the *Fermi* Bubbles.

Together with the secondary leptons, the hadronic model can describe the gamma-ray emission observed from the *Fermi* Bubbles similar to the leptonic model (Ackermann, Albert, et al. 2014).

3.2 Origin of the *Fermi* Bubbles

As discussed in Su et al. 2010 there are two popular models to describe how the *Fermi* Bubbles are created. One possible explanation could be an active past of the SMBH Sgr A* located in the centre of our galaxy. Another explanation could be a nuclear starburst event in the past 10 Myr near the GC. Both scenarios are possible and might be responsible for the formation of the *Fermi* Bubbles individually or in cooperation.

3.2.1 Active Past of the Galactic Center

The formation of the *Fermi* Bubbles due to an active past of the SMBH Sgr A* located at the GC is one possible explanation. In this active time the SMBH could be responsible for an energy injection, e.g., due to a relativistic jet. Such relativistic jets can accelerate CRs to high energies and therefore could be considered as the source of the gamma-ray emission of the *Fermi* Bubbles. If one assumes the leptonic model, the homogeneous energy spectrum within the *Fermi* Bubbles and the observed sharp edges favours this specific scenario (Ackermann, Albert, et al. 2014).

The age of the *Fermi* Bubbles can be estimated by assuming IC scattering of the ISRF by 10 GeV to 100 GeV CR electrons as the primary emission process. This estimation leads to an upper limit of a few Myr (Su et al. 2010). Therefore, the spatial uniform spectrum of the *Fermi* Bubbles requires efficient particle transport from the source to the place where the gamma-ray emission is observed today. This can be achieved by jets of an AGN and is shown in Yang et al. 2012 by three-dimensional magnetohydrodynamic simulations of the *Fermi* Bubbles with CR jet injections.
In addition, AGN jets are candidates for bubble-like structures observed in massive galaxies, e.g., the giant elliptical galaxy NGC 5128 (figure 7), and galaxy clusters (McNamara et al. 2007; Laing et al. 2006). Because of limited sensitivity and resolution, it is hard to detect the gamma-ray emission from these objects, but the *Fermi* Bubbles, a bubble-like structure in our own galaxy, can possibly help to investigate the gamma-ray band of such structures.

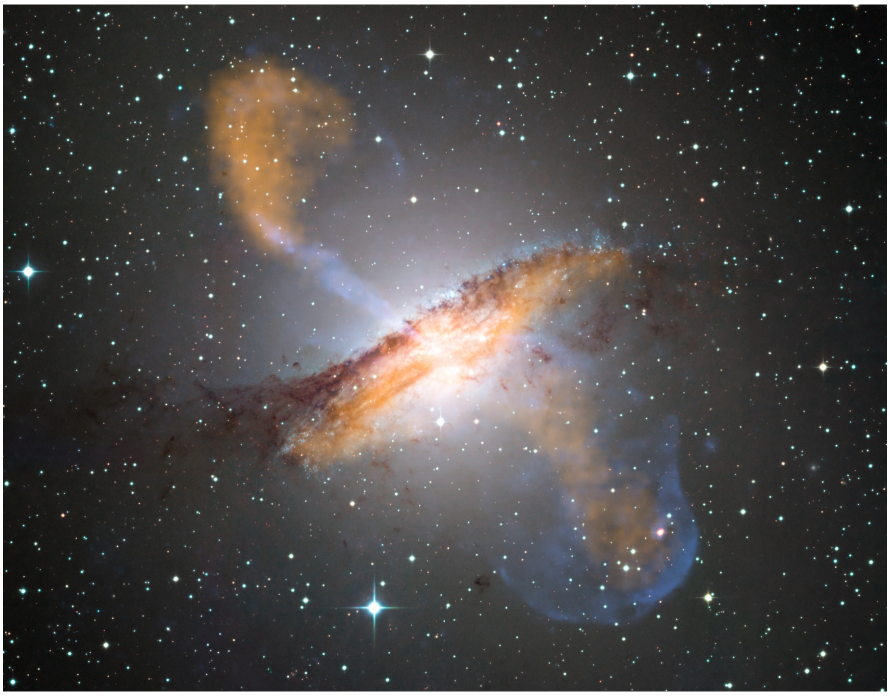

Figure 7: The active galaxy NGC 5128, or Centaurus A, in a composition of different wavelength. The data from the submillimetre (orange) and X-ray (blue) band reveal a bubble-like structure. The jet originating from the central black hole of the galaxy can also be seen. Optical data shows the surrounding dust and background stars. Figure taken from ESO April, 2018.

3.2.2 Starbursts and Stellar Winds

In this scenario the vast amount of energy is injected into the volume of the *Fermi* Bubbles by a period of starburst activity, or stellar winds driven by a long time and high areal density star formation near the GC (Crocker et al. 2011). There is evidence of around 40 OB supergiant stars within the central 0.5 pc of our galaxy (Paumard et al. 2006). The age of these stars is estimated to 6 Myr and therefore fits to the estimated age of the *Fermi* Bubbles. In simulations (Sofue et al. 2001) and observations of some starburst galaxies, like the M82 (figure 8), bubble-like structures can be found.

Figure 8: The galaxy M82 showing a bubble-like structure in the low energy X-ray data from NASA's Chandra X-ray Observatory (blue). Higher energy X-ray data from NuSTAR (pink) shows mighty pulsar (magenta) in the center. Visible light shows the surrounding dust and background stars. Figure taken from NASA April, 2018.

As proposed in Cheng et al. 2011 periodic star capture processes by Sgr A* can also explain the origin of the *Fermi* Bubbles. A capture rate of $3 \times 10^{-5}\,\mathrm{yr}^{-1}$ and an energy release of around 3×10^{52} erg per capture can lead to shocks in the halo which accelerate electrons to energies up to some TeV. These electrons are able to produce gamma-ray photons via IC scattering.

An alternative approach to the two scenarios mentioned before is presented in Zubovas et al. 2011, where the *Fermi* Bubbles are the relic of an outflow from the SMBH. They argue that this outflow is a natural result of a short but bright accretion event onto Sgr A*. Furthermore, they claim that this event happened concurrently with the star formation reported in Paumard et al. 2006. This approach is a combination of the starburst and stellar wind scenario and an active past of the SMBH.

3.3 Low-Latitude *Fermi* Bubbles

The main challenge of the low-latitude *Fermi* Bubbles analysis is the spatial overlap with other components of galactic gamma-ray emission, which are considered as the gamma-ray background. Compared to these components the *Fermi* Bubbles are faint. The second issue would be the discrimination of the *Fermi* Bubbles from the observed GC excess (Goodenough et al. 2009; Vitale et al. 2009; Ackermann, Ajello, et al. 2017) which can be associated with Dark Matter annihilation or millisecond Pulsars around the GC. In addition, the *Fermi* Bubbles are a large-scale extended source. At low latitudes the *Fermi* Bubbles might be more narrow but still covering nearly the whole FOV. Most of the current analysis chains are focused on point-like sources. Therefore, an analysis strategy is needed to distinguish faint extended sources from other bright sources.
The first step is to estimate the sensitivity of CTA to extended sources like the *Fermi* Bubbles. For this purpose the FOV is divided into an on-region, covered by an extended source and a background region, the so called off-region, where no extended source is expected. The on-region is defined as the half of the FOV, consequently the off-region has the same size as the on-region. If one considers the extended source as the sum of point sources and claim that the statistical significance for the extended source is equal to the statistical significance for the point source, the estimated sensitivity for extended sources has the form

$$I_{\mathrm{ext}} = \frac{F_{\mathrm{ext}}}{\Omega_{\mathrm{ON}}} = \frac{F_{\mathrm{ps}}}{\sqrt{\Omega_{\mathrm{PSF}} \cdot \Omega_{\mathrm{ON}}}}, \tag{2}$$

where F_{ext} and F_{ps} is the flux of the extended source and point source respectively. The size of the point spread function [2] (PSF) is denoted by Ω_{PSF} and the area of the on-region is referred to as Ω_{ON}. For more details see Appendix A. Figure 9 shows the estimated extended source sensitivity of CTA based on the point source sensitivity for different observation times.
According to Ackermann, Ajello, et al. 2017 the spectrum of the low-latitude *Fermi* Bubbles is harder compared to higher latitudes and its exponential cut-off energy is possibly larger than mentioned before, i.e., $E_{\mathrm{cut}} \geq 110\,\mathrm{GeV}$. A possible spectrum is shown in figure 9. Because of the harder spectrum, CTA should be sensitive to the low-latitude *Fermi* Bubbles with its sensitivity of 5 h. Therefore, it would be interesting, especially for low latitudes, to observe the *Fermi* Bubbles at higher energies where the *Fermi*-LAT loses sensitivity. In addition to the harder spectrum, some analyses of the *Fermi*-LAT data shows that the southern *Fermi* Bubbles are asymmetric with respect to the GC, i.e., for negative longitudes the *Fermi* Bubbles are brighter than for positive longitudes. Figure 10 (a) shows the *Fermi* Bubbles template derived from the *Fermi*-LAT data (Ackermann, Ajello, et al. 2017). At low latitudes the *Fermi* Bubbles are brighter and if one has a closer look to the southern *Fermi* Bubbles the asymmetry is visible (figure 10 (b)).

---

[2] describes the response of an imaging instrument to a point source

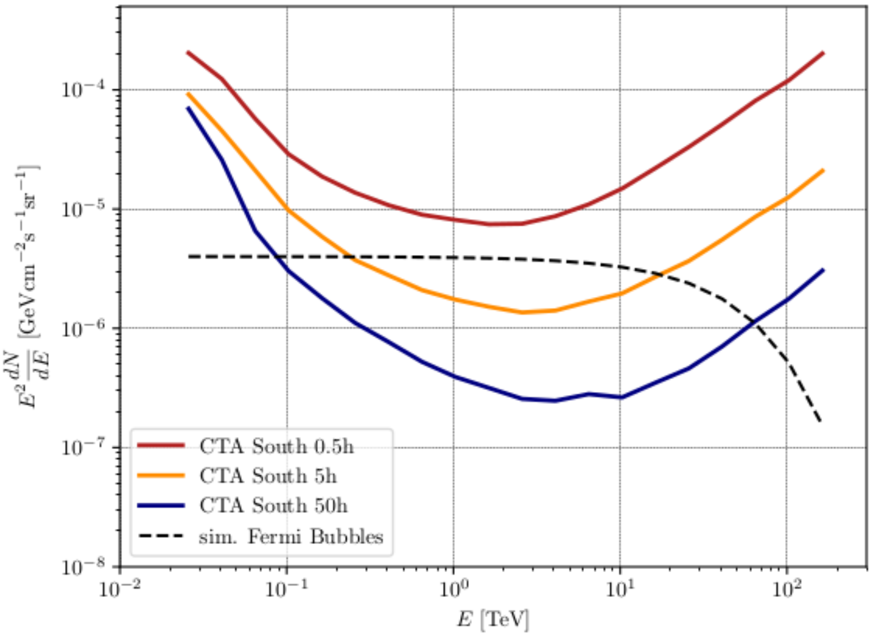

Figure 9: Estimated sensitivity to extended sources of CTA-South for different observation times (red, orange, blue). The estimation is done by using the PSF for a point source and assuming the extended source cover the half of the FOV. The black dashed line shows the assumed spectrum of the low-latitude *Fermi* Bubbles based on Ackermann, Ajello, et al. 2017. With this rough estimation CTA is already sensitive to the low-latitude *Fermi* Bubbles with its sensitivity curve of 5 h.

4 The first CTA Data Challenge

The first CTA data challenge (1DC) is designated for the CTA Consortium Science Working Groups to derive the performance of developed software, like *ctools* and *GammaLib* (IRAP March, 2018), and analysis chains on simulated data. The 1DC should provide first estimates for CTA's capabilities to achieve the different science goals. Therefore, results of the 1DC should be spectra, light curves or images of gamma-ray emitting objects that illustrate the CTA science cases. Distributed data in the 1DC are high level data which contains event lists and instrument response functions (IRF). Event lists comprise reconstructed properties, e.g., energy of the observed events. These event lists were simulated from high level IRF coming with the 1DC. The IRF describes the transformation from physical properties of the incident photons to the measured characteristics of a single event and corresponds to an ideal CTA with good and stable atmosphere and instrument conditions. Data, provided by the 1DC, are simulated for all key science projects namely the galactic plane and centre survey as well as the extragalactic survey using realistic pointing patterns. A short description of the used software and simulated data can be found in the next section.

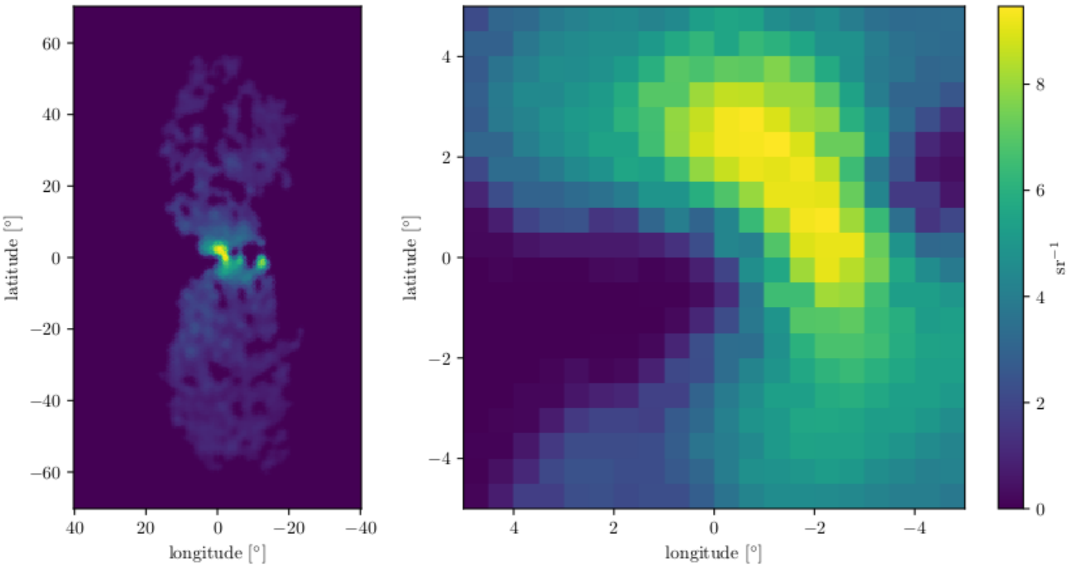

(a) *Fermi* Bubbles template. (b) low-latitude *Fermi* Bubbles.

Figure 10: (a) shows the template of the *Fermi* Bubbles derived from the *Fermi*-LAT data. At low latitudes, i.e., $|b| \leq 10°$, the *Fermi* Bubbles are brighter. (b) shows the asymmetry of the southern low-latitude *Fermi* Bubbles with respect to the GC.

4.1 Software

The software package *ctools* (Knödlseder et al. 2016) is used to simulate and analyse gamma-ray data. This software is based on the *GammaLib* library (Knödlseder et al. 2016), developed to support the analysis of high level gamma-ray data. The *ctools* package is written in C++ and Python and can either be used from the command line via shell scripts or from a Python script. A definition of the IRF is needed to simulate and analyse data with *ctools*. In *ctools* the IRF is defined by two parameters namely the calibration database (`caldb`) and the name of the IRF (`irf`). Both come with the 1DC and will undergo further development. For this work the calibration database `caldb` = `1dc` and the IRF called `irf` = `South_z20_50h` is used. The IRF is therefore optimised for the CTA-South with a zenith angle of $z = 20°$ and an observation time of $t_{\mathrm{obs}} = 50\,\mathrm{h}$. *ctools* provides several tools to simulate and analyse data. In the following a short description of some tools used in this work is given. For more details see Knödlseder et al. 2016.

`ctobssim` simulates event lists based on an input model and the characteristics of the instrument provided by the IRF. A general model in *ctools* is described by three different components which are defined in a model definition file. The entire model consists therefore of the spatial M_{S}, spectral M_{E} and temporal model M_{T}:

$$M(x, y, E, t) = M_{\mathrm{S}}(x, y) \cdot M_{\mathrm{E}}(E) \cdot M_{\mathrm{T}}(t). \tag{3}$$

The simulated events include events from astrophysical sources and the background defined in the input model. The background is generated based on the input model using the numerical random number generator of the *GammaLib* library.

`ctbin` bins the simulated events into different energy bins. Therefore, this tool creates a three-dimensional data cube spanned by right ascension or galactic longitude, declination or galactic latitude and reconstructed energy.

`ctmodel` generates a three-dimensional data cube, similar to `ctbin`, but with the number of predicted counts for a certain input model as a function of reconstructed right ascension or galactic longitude, declination or galactic latitude and energy at the output.

`ctlike` allows the determination of the flux, spectral index, position or extension of a gamma-ray source by applying a maximum likelihood model fitting to the data. `ctlike` requires an input model where all free model parameters are adjusted. At the output `ctlike` creates an output model, similar to the input model, which contains the best fit values for each free parameter.

The last tool discussed here is the `csspec` tool. This script extracts the spectrum of a given gamma-ray source in units of $\mathrm{erg\,cm^{-2}\,s^{-1}}$ by fitting an input model for a given energy range to the data.

4.2 Data Simulation and Modelling

Simulations done with *ctools* are based on the galactic centre survey model definitions coming with the 1DC, except for the *Fermi* Bubbles. As discussed in section 3.3 the spectrum of the low-latitude *Fermi* Bubbles is assumed to be harder compared to the higher latitude *Fermi* Bubbles and extend above 1 TeV (figure 9). Therefore, the spectrum of the *Fermi* Bubbles in the galactic centre survey model definitions is modified. The spectrum of the simulated low-latitude *Fermi* Bubbles is an exponential cut-off power low of the form

$$M_{\mathrm{E}} = k_0 \left(\frac{E}{E_0}\right)^{-\gamma} \exp\left(\frac{-E}{E_{\mathrm{cut}}}\right), \tag{4}$$

where $\gamma = 2$, $k_0 = 1 \times 10^{-10}\,\mathrm{MeV^{-1}\,cm^{-2}\,s^{-1}}$, $E_0 = 1 \times 10^3\,\mathrm{MeV}$ and $E_{\mathrm{cut}} = 50\,\mathrm{TeV}$. The values for γ, k_0 and E_0 are adopted from Ackermann, Ajello, et al. 2017. E_{cut} is an arbitrary value above 1 TeV, because this energy cut-off is not proven to date. The spatial model of the *Fermi* Bubbles (figure 10) is exactly the same as in the 1DC which is based on the *Fermi*-LAT data (Ackermann, Ajello, et al. 2017). There is no time variation of the *Fermi* Bubbles, i.e., M_{T} is constant. With this model of the GC including the model of the low-latitude *Fermi* Bubbles, there are three different types of simulations: One simulation contains only the different sources within the GC, the gamma-ray background, i.e., everything of the galactic centre survey model is included in the simulation but no general background referred to as the CR background. This type of simulation is called the GCNB-simulation which is used to test the analysis chain and different algorithms developed in this work. The second type of simulation contains all GC sources, meaning the gamma-ray background, except for the *Fermi* Bubbles and

identifier	model	t_{obs}
GCFB	GC+FB+BKG	5 h and 50 h
GCNB	GC+FB−BKG	5 h and 50 h
GCNF	GC−FB−BKG	5 h and 50 h

Table 1: Summary of the different simulation types together with the time of the observation t_{obs}. The included/excluded models are indicated with (±). The identifier GCFB stands for a simulation of the GC including the *Fermi* Bubbles and background. The identifier GCNB denotes a simulation of the GC including the *Fermi* Bubbles but no background and the identifier GCNF stands for a simulation of the GC but no *Fermi* Bubbles and background. The GC and the BKG model is exactly the same as in the 1DC. The model of the *Fermi* Bubbles (FB) consists of an exponentially cut-off power law (spectral model) and the *Fermi* Bubbles template (spatial model) derived in Ackermann, Ajello, et al. 2017.

CR background. This is referred to as the GCNF-simulation and is needed to check if the tested analysis chain detects a signal from the *Fermi* Bubbles if there is no *Fermi* Bubbles input in the simulated data. Finally, the whole GC is simulated including the low-latitude *Fermi* Bubbles as well as the entire background. This simulation is referred to as the GCFB-simulation. The use of this simulation type is needed to test the analysis in a more realistic situation. A summary of the different simulation types is shown in table 1. According to section 3.3, CTA is sensitive to the low-latitude *Fermi* Bubbles for observation time $t_{\mathrm{obs}} \geq 5\,\mathrm{h}$. Therefore, the different simulation types are simulated for 5 h and 50 h only. In chapter 5 the focus is on the 50 h simulations. Appendix C shows the analysis applied to the 5 h data just for completeness. The pointing of the telescopes in the simulated data is towards the GC and the FOV is assumed to be 10° in size. A single pixel of the simulated data has a size of 0.02°. Figure 11 shows two examples of simulated data, namely the GCFB- and GCNB-simulation both with $t_{\mathrm{obs}} = 50\,\mathrm{h}$.

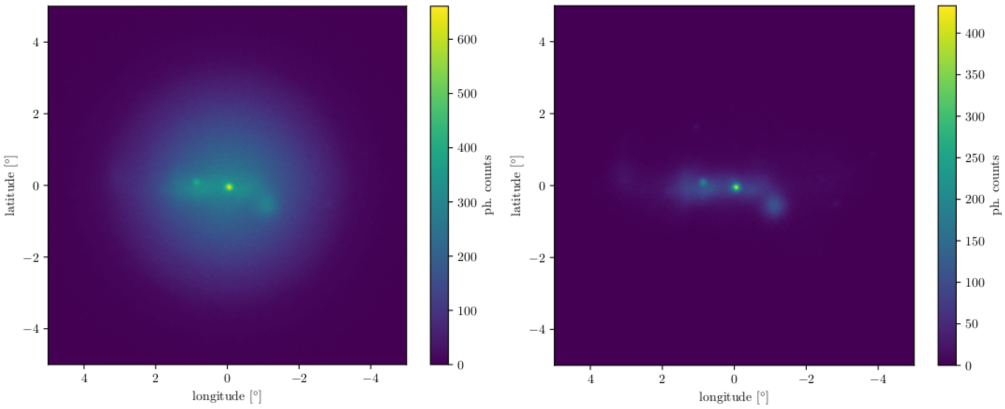

(a) GCFB (b) GCNB

Figure 11: Two examples of simulated data of the GC. The observation time of both simulations is $t_{\mathrm{obs}} = 50\,\mathrm{h}$. (a) simulation of the GC including *Fermi* Bubbles gamma- and CR background, referred to as the GCFB-simulation. (b) simulation of the GC including *Fermi* Bubbles and gamma-ray background but no CR background, referred to as the GCNB-simulation.

5 Detecting the *Fermi* Bubbles with CTA

This main chapter describes the strategy to analyse the low-latitude *Fermi* Bubbles with CTA. The selection of a proper region of interest (ROI) is described in section 5.1 and is the first step in the analysis. To discriminate the *Fermi* Bubbles from other gamma-ray sources, the so called spectral component analysis (SCA) is applied to the data. The principle of this method is described in section 5.2. After applying the SCA, an on-off analysis is performed in section 5.3 to detect a signal from the *Fermi* Bubbles. Section 5.4 describes a method to create an output template of the *Fermi* Bubbles which can be used for further analysis.

5.1 Selection Strategy for the Region of Interest

As described in section 3.3 the *Fermi* Bubbles are brighter at lower latitudes ($|b| < 10°$) than at higher latitudes. Additionally, the southern low-latitude *Fermi* Bubbles are asymmetric with respect to the GC. These two aspects can be used to define a ROI such that the on-off analysis can be applied later.

5.1.1 Selecting the On- and Off-Region

Assuming the morphology of the *Fermi* Bubbles, revealed by the *Fermi*-LAT data (figure 10), a background region, also called off-region, is defined for positive longitudes ($l > 0$). In the off-region no *Fermi* Bubbles are expected, or their brightness is significantly reduced compared to the *Fermi* Bubbles in the on-region. The on-region is defined for negative longitudes ($l < 0$), i.e., mirrored at the vertical axis $l = 0$. In the following the sum of the on- and off-region is called the ROI. The ROI can be divided into different latitude bands (b-band). Each b-band is defined by $b_1 < b < b_2$, where b_1 and $b_2 = b_1 + \Delta b$ is called the lower and upper bound of the b-band, respectively. Δb is referred to as the band width. Moreover, the b-band can be divided into several subregions. These subregions are called on- or off-pixels. The photon counts within such an on- or off-pixel are summed up to

$$N_j = \sum_{i \in j} n_i, \tag{5}$$

where N_j denotes the sum of photon counts in each on- or off-pixel j and n_i represents the photon counts detected in one pixel i of the simulated data, which is part of the on- or off-pixel. This procedure is illustrated in figure 12.

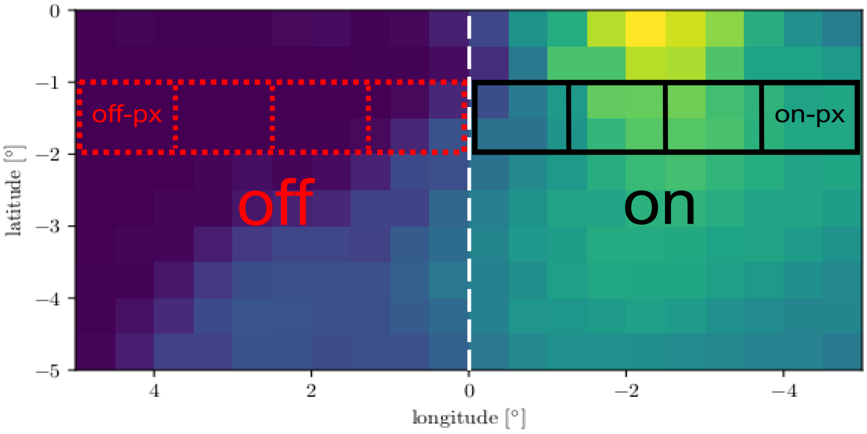

Figure 12: Illustration of the on-region selection strategy. The selection strategy uses the asymmetry of the southern low-latitude *Fermi* Bubbles. The off-region (red) marks a region where no *Fermi* Bubbles are expected, or their brightness is significantly reduced compared to the on-region. The on-region (black) itself is defined as the mirrored off-region. The axis of reflection is the vertical dashed line at $l = 0$ (white). Each region can be divided into several subregions, so called on- or off-pixels. The ROI is defined by adding the on- and off region. This ROI can divided into different b-bands. In this picture only one b-band is shown.

5.1.2 Source Contributions

To get an impression of the background overlapping the *Fermi* Bubbles in the on- or off-region, a GCFB-simulation of 50 h is considered. Figure 13 shows the longitude profile of the main source contributions (gamma-ray background) in a certain b-band ($b_1 = -2.5°, b_2 = 2.0°, \Delta b = 0.5°$) together with the *Fermi* Bubbles. Each data point represents an off-pixel of the off-region (figure 13 (a)) or an on-pixel of the on-region (figure 13 (b)). The expected photon counts of the gamma-ray background and the *Fermi* Bubbles are calculated using `ctmodel`. The difference between the total data N_j and the total model M_j in each on- or off-pixel implies the background coming from CR for example. Where

$$M_j = \sum_{\mu} \sum_{i \in j} m_i^{\mu} \tag{6}$$

is the sum of expected photon counts of all source contributions μ in each on- or off-pixel j and m_i^μ represents the expected photon counts of each source contribution in each pixel i of the modelled data. The CR background dominates each pixel and is some orders of magnitudes larger than the expected photon counts from the *Fermi* Bubbles. Moreover, some source contributions of the gamma-ray background are brighter or at least similar to the *Fermi* Bubbles in most pixels. Applying an on-off analysis to the selected regions, requires a radial symmetric background. This is equal to a symmetric background with respect to the vertical axis at $l = 0$. If some source contributions break this symmetry in considered on- or off-pixels significantly, the on-off analysis does not work properly in these pixels. Figure 13 shows that indeed there are source contributions breaking this symmetry, e.g., the SNR contribution. Consequently, the on-off analysis cannot be applied to the data directly, except the background can be modelled very well and can therefore be subtracted from the data. Hopefully, CTA will also improve the modelling of gamma-ray sources overlapping the *Fermi* Bubbles by observing the GC region and revealing new sources or improve the understanding of known sources. But this is not part of this work. Therefore, an analysis is needed to distinguish the *Fermi* Bubbles from most of the other sources.

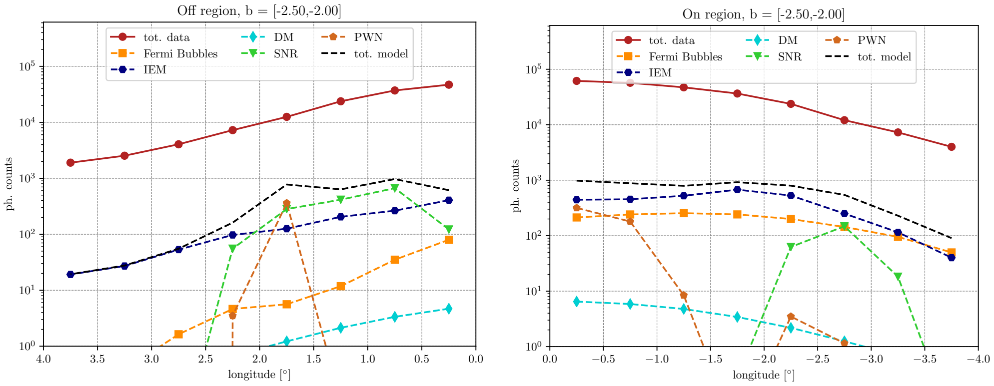

(a) off-region

(b) on-region

Figure 13: Longitude profiles of different source contributions in a certain latitude band including: The Interstellar Emission Model (IEM), Supernova Remnants (SNR), Pulsar Wind Nebulae (PWN), Dark Matter (DM) and the *Fermi* Bubbles. In this particular example, a GCFB-simulation of 50 h is used and latitudes of −2.5° to −2.0° are considered. For most longitudes the *Fermi* Bubbles have less or similar counts than other sources. But in the on-region (b) the *Fermi* Bubbles are brighter compared to the off-region (a), i.e., here the asymmetry of the southern low-latitude *Fermi* Bubbles is shown. Also other sources, like the SNRs, break the symmetry with respect to the vertical $l = 0$ axis.

5.2 Spectral Component Analysis

The analysis used to distinguish the *Fermi* Bubbles from most of the background sources is called the spectral component analysis (SCA). It was developed to separate the components of a diffuse emission process based on their energy spectra (Malyshev 2012). This analysis is semi-blind, that means it is sufficient to assume a functional form of the energy spectrum for each component and derive the parameter by minimizing the χ^2 function for instance. The SCA has two assumptions: First of all it assumes that the energy spectra of the different components have a functional form. The second assumption is that the spatial distribution of each component does not depend on the energy.
In the following sections the principle of the spectral component analysis and the influence of some free parameters, which affect the outcome of the SCA, are introduced. Furthermore, remaining problems with respect to the analysis of the *Fermi* Bubbles are discussed.

5.2.1 The Principle of the SCA

The different components of the diffuse emission can be modelled by a linear combination of the data $d_{i\alpha}$ in different energy bins α. Only two components are needed to distinguish the *Fermi* Bubbles from most of the background sources. The first component contains the low-latitude *Fermi* Bubbles. This component has a hard exponential cut-off power law spectrum with an index of $\gamma_h = 2.0$ and a cut-off energy of $E_{\text{cut}} = 50\,\text{TeV}$, as shown in section 3.3. This is referred to as the hard component. The second component, the so called soft component, consists in principle of the whole background, meaning the sum of the gamma-ray and CR background. This soft component is modelled by a power law. The index γ_s of the soft component is a free parameter which has to be chosen such that this component absorbs most of the background sources. Therefore, the index of the soft component is expected to has a big impact on the outcome of the SCA. The modelled SCA data $m_{i\alpha}$ of the two components can therefore written as

$$m_{i\alpha} = H_i \cdot \phi_\alpha + S_i \cdot \varphi_\alpha, \tag{7}$$

where H_i and S_i are the unknown normalization factors of the hard and soft component, respectively. The functional form ϕ of the hard component is defined as

$$\phi_\alpha = \exp\left(\frac{-E_\alpha}{E_{\text{cut}}}\right) E_\alpha^{-\gamma_h} \tag{8}$$

and the functional form φ of the soft component is defined as

$$\varphi_\alpha = E_\alpha^{-\gamma_s}, \tag{9}$$

where E_α is the energy of the energy bin center. The unknown normalization factors H_i and S_i can be found by minimizing the χ^2 function

$$\chi^2 = \sum_{i\alpha} \frac{(d_{i\alpha} - m_{i\alpha})^2}{\sigma_{i\alpha}^2}, \tag{10}$$

where $\sigma_{i\alpha}^2$ is the variance. Inserting equation (7) into equation (10) and calculating the first derivative with respect to H_i and S_i, lead to a minimization problem which is linear in H_i and S_i. According to Sivia et al. 2006 the uncertainties of H_i and S_i can therefore be calculated using the Hessian matrix of the linear minimization problem. For more details see Appendix B.

Due to the matter of counting single photons in each pixel i the statistics are based on Poisson statistics. As a result the variance is equal to the mean number of photons in each pixel. In this case it holds that

$$\sigma_{i\alpha}^2 = d_{i\alpha}. \tag{11}$$

Hence, pixels with zero counts are problematic. This problem appears especially at high energies. To avoid pixels with zero counts the size of the pixel can be enlarged. But larger pixels reduce the possibility to detect the morphology of the low-latitude *Fermi* Bubbles. Therefore, a proper agreement between the pixel size, needed for the SCA to avoid zero counts, and the pixel size, needed to detect the morphology of the *Fermi* Bubbles, is necessary. In the next section this will be described in more detail. Another procedure is to reduce the number of energy bins. The SCA needs at least some energy bins to distinguish the different components because of their energy spectra. The number of energy bins is set to $\alpha = 20$.

Moreover, the SCA operates properly if the energy spectra of the diffuse components are completely different compared to each other. The SCA is not able to discriminate components with similar energy spectra. It is expected to have contributions to the hard component coming from other sources than the *Fermi* Bubbles.

The results of the spectral component analysis are two count maps, one for the hard and one for the soft component. In each pixel of these maps the photon counts associated with the corresponding component integrated over the energies is shown. Hence, the energy information in each pixel is lost, but the aim of the SCA is to filter out the *Fermi* Bubbles from the data only. The hard component map will be used as a basis for the spatial model of the detected *Fermi* Bubbles later. Figure 14 shows an example of how the hard and soft component could look like. The data simulation used to generate these count maps is a GCNB-simulation of 50 h. To reveal more structure in these two count maps, a latitude band of $-1° < b < 1°$, hosting bright sources, is masked.

The hard component map (figure 14 (a)) with an index of $\gamma_h = 2.0$ shows the asymmetry of the southern low-latitude *Fermi* Bubbles. As expected there are contributions to the hard component map which do not belong to the *Fermi* Bubbles. For instance, the four brighter pixels around $(l, b) = (-0.5°, -2.5°)$ are on top of the *Fermi* Bubbles. Therefore, these four pixels considered as an outstanding source (S_1) contributing to the hard component. Using the hard component map as the basis of the spatial model of the detected *Fermi* Bubbles, these kind of background sources would lead to an overestimated signal. This problem is solved in section 5.4.

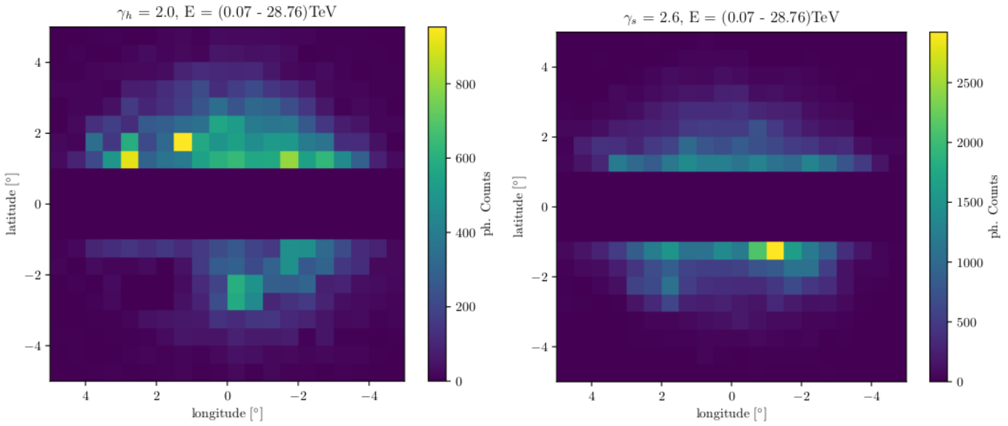

(a) hard component

(b) soft component

Figure 14: (a) the hard component map as a result of the SCA applied to the simulated data of a 50 h GCNB-simulation. A latitude band of $-1° < b < 1°$ is masked to show more interesting structures. The index is $\gamma_h = 2.0$ and the energy range for the SCA is ranging from 0.07 TeV to 28.76 TeV. The asymmetry with respect to the vertical axis $l = 0$ at negative latitudes is visible. There are some remaining source contributions which do not come from the *Fermi* Bubbles. (b) the corresponding soft component map using the same conditions like the hard component map but an index of $\gamma_s = 2.6$. Compared to the hard component map, the soft component map is nearly complementary. Bright regions in the soft component are darker regions in the hard component map.

The soft component map (figure 14 (b)) with an index of $\gamma_s = 2.6$ is nearly complementary to the hard component map. Brighter regions in the soft component map are darker regions in the hard component map. The overall brightness of the soft component is higher by a factor of approximately three. This indicates that most of the background is absorbed into the soft component. It is possible that the soft component has also some contributions from the *Fermi* Bubbles, but this contribution is expected to be low compared to the *Fermi* Bubbles contribution to the hard component. As a foresight to deal with real data and also not knowing the spectrum of the low-latitude *Fermi* Bubbles in great detail, it is essential to test how the changes in parameters affect the outcome of the SCA. More about the influence of different parameters is described in the next section. Furthermore, in the following sections only negative latitudes are considered, i.e., the focus is on the southern low-latitude *Fermi* Bubbles. From now on the ROI is defined as the area spanned from $-4°$ to $4°$ in longitude and from $-4°$ to $-1°$ in latitude.

5.2.2 Determination of SCA Parameters

As already mentioned before, the SCA does not work for pixels containing zero photon counts, referred to as zero pixels. To reduce the number of zero pixels, the size of a single pixel (pxs) can be increased. Thus, the solid angle $d\Omega$ of this particular pixel will be larger. That means a single pixel covers a larger area on the sky and, therefore, gather more photons. But a larger pixel size lead to a lower spatial resolution. Concerning the morphology of the *Fermi* Bubbles, a proper pixel size has to be found such that the number of zero pixels are low while the spatial resolution is high enough to detect the morphology of the low-latitude *Fermi* Bubbles as well. To ensure that the SCA works properly, the number of zero pixels must be minimized. Therefore the number of zero pixels is counted in each energy bin depending on the pixel size of a single pixel. The pixel size of the simulated data is 0.02°. With the FOV = 10° the data has 250 000 pixels. The pixel size used in the SCA should be $\text{pxs} = n \cdot 0.02°$ with $n \in \mathbb{N}$. Here $n \in \{10, 20, 25, 50\}$ is used to show the dependency between the pixel size and the energy. Figure 15 shows the number of zero pixels over the energy. The number of zero pixels decreases from the low to the mid energy range. This is due to the fact, that the simulated data is in rectangular shape of $(10 \times 10)°$, but the FOV is a circle with a radius of 5°. Consequently, there are no photon counts in the corners of the simulated data (figure 11). In addition, the effective area decreases with energy, i.e., CTA detects less photons at lower energies for a certain flux. After reaching its minimum at around 4 TeV the number of zero pixels increases with increasing energy more rapidly. At higher energies the number of zero pixels is larger, because at higher energies one expects also less photon counts due to a lower flux. This could lead to additional zero pixels.

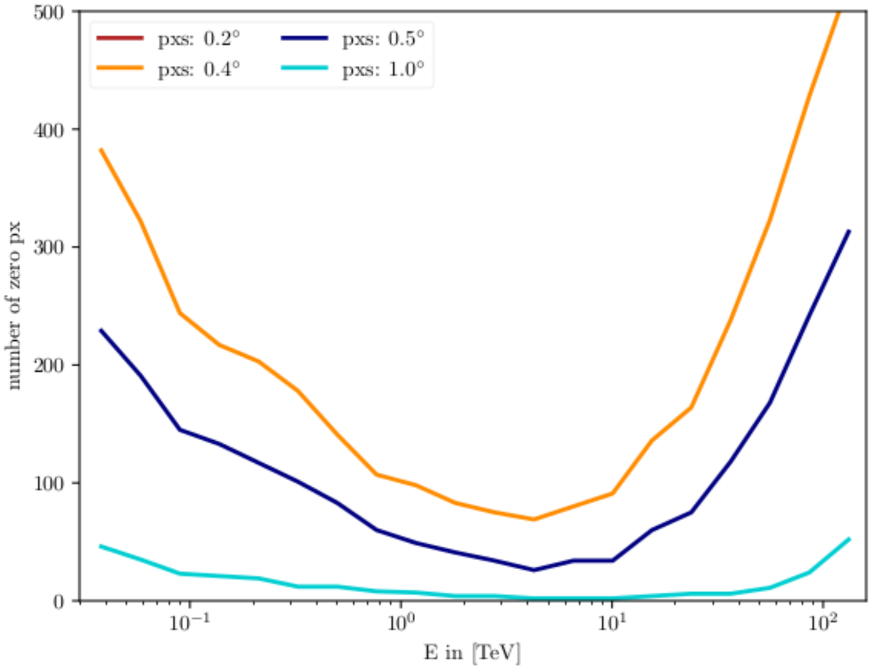

Figure 15: The number of zero pixels depending on the pixel size of a single pixel and the energy. Different pixel sizes are color coded. The pixel size of 0.2° (red) is out of the plotted number of zero pixel range. The number of zero pixels at low energies decreases until it reaches a minimum at around 4 TeV. These zero pixels come from the fact, that the simulated data is in rectangular shape whereas the FOV is a circle. To higher energies the number of zero pixels increases more rapidly, because of the lower flux which could cause zero pixels.

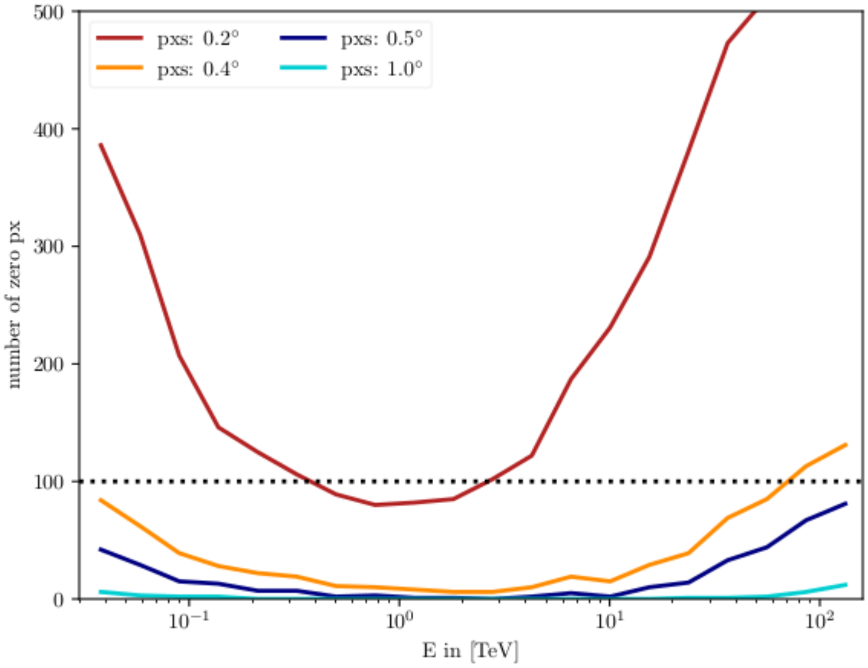

Figure 16: The number of zero pixels depending on the pixel size of a single pixel and the energy again but in a restricted area of $-4° < l < 4°$ in longitude and $-4° < b < -1°$ in latitude (ROI). Different pixel sizes are color coded. The effect of zero pixels at lower energies is reduced. An arbitrary threshold of 100 zero pixels (dashed black line) is introduced to determine the pixel size. For a pixel size smaller than 0.5° the number of zero pixels is below the threshold for all energies.

To reduce the number of zero pixels, especially at lower energies, the SCA is restricted to the defined ROI. Figure 16 shows the number of zero pixels in the ROI depending on the pixel size and energy. The effect of counting zero pixels due to the rectangular shape of the simulated data at low energies is significantly reduced. An arbitrary threshold of 100 zero pixels is introduced now to determine the pixel size used in the SCA. In principle this threshold is just for visualization. For a pixel size smaller than 0.5° the number of zero pixels stay below the threshold for all energies. Furthermore, the blue line in figure 16, which corresponds to a pixel size of 0.5°, reaches nearly zero in the energy range from 0.4 TeV to 10 TeV. As a result the pixel size for the SCA is set to 0.5° and the energy range is set from 0.39 TeV to 12.19 TeV. The lower and upper bound of this energy range is fixed due to the edges of the energy bins.

The most important parameter of the SCA is the index γ of each component. Together with the spectral form it is the single assumption used as an input parameter. One has to make an educated guess how the spectrum of a certain component could look like. In the following observations the component of interest is the component of the low-latitude *Fermi* Bubbles. According to former investigations (Ackermann, Ajello, et al. 2017) the low-latitude *Fermi* Bubbles have a significant harder spectrum compared to the *Fermi* Bubbles at higher latitudes. The index is assumed to be around $\gamma = 2$. Therefore, the hard component index is fixed to $\gamma_h = 2.0$. Only two components are used, i.e., the outcome of the SCA strongly depends on the second input parameter, namely the soft component index. It is extremely important to test the input parameter and the influence of the same parameter with regard to deal with real data and to interpret the SCA results.

To investigate the influence of the soft component index γ_s, a GCNB-simulation of 50 h is used. The soft component index will be altered from 2.3 to 2.7 in steps of $\Delta\gamma = 0.2$. It is expected that all sources with an index of $\gamma < \gamma_h$ or $\gamma_s < \gamma$ contribute only to the hard or soft component, respectively. Whereas sources with an intermediate index of $\gamma_h \leq \gamma \leq \gamma_s$ contribute to both components. The closer the index of a particular source is to one of the indices γ_h or γ_s, the larger the expected contribution. Consequently, if γ_h and γ_s are close to each other the correct matching of intermediate sources could be problematic. The resulting count maps will be compared. If the maximum residual is smaller than 5% the SCA run is accepted. Furthermore, a residual count map will be used to quantify the quality of the SCA run. The residuals are defined as

$$r_i = \sum_{\alpha}(d_{i\alpha} - m_{i\alpha}). \tag{12}$$

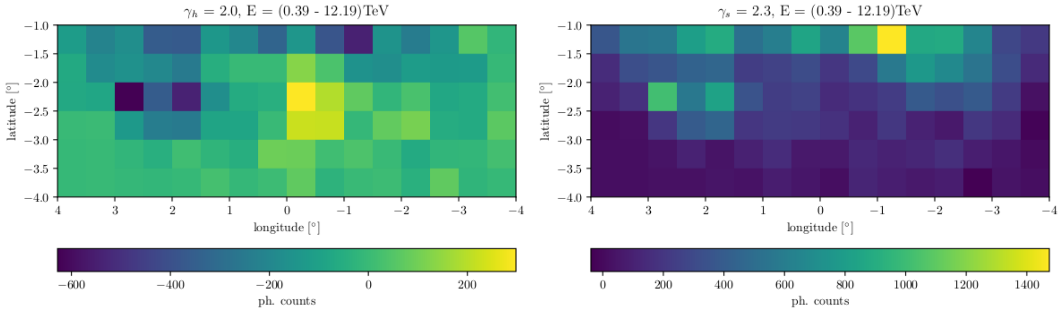

(a) hard component (b) soft component

Figure 17: The hard and soft component maps of the SCA using the index configuration $\gamma_h = 2.0$ and $\gamma_s = 2.3$. (a) the hard component is mostly negative (blue). Only very hard components survive in the hard component map (yellow) because γ_h is close to γ_s. (b) the soft component contains most of the photons but is overestimating the soft component because there are also contributions from hard components.

Figure 17 shows the result of the SCA using $\gamma_s = 2.3$ which is close to $\gamma_h = 2.0$. The hard component (figure 17 (a)) has a lot of negative pixel values (blue). In these pixels the SCA relates most of the photon counts to the soft component. This can be explained by the similar indices γ_h and γ_s and the fact that most sources have an index of $\gamma_s < \gamma$. In addition to the quite negative pixels there are some positive pixel values which are close to zero (green). Hence, the SCA detects only a few photons belonging to the hard component in these pixels. That does not necessarily mean that there are no sources with a hard spectral fraction.

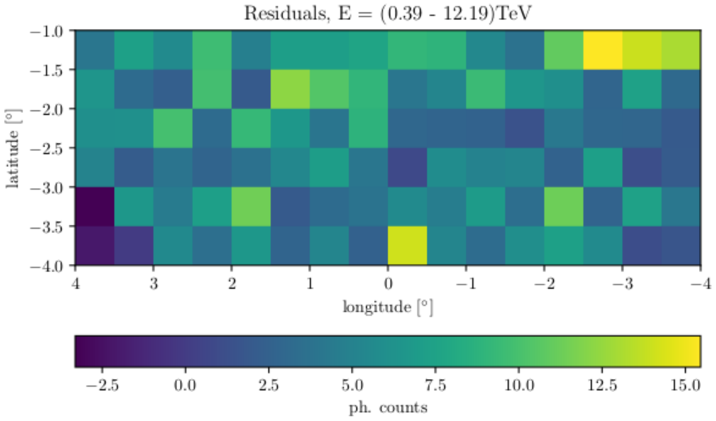

Figure 18: Residuals in each pixel integrated over the energy range used in the SCA. The index configuration is $\gamma_h = 2.0$ and $\gamma_s = 2.3$. Overall the residual map has low residuals. The mean residual is 6 photon counts. The maximum deviation from the simulated data is around 3%.

The bright pixels (yellow) reveal a source with a clear hard contribution, i.e., probably $\gamma < \gamma_h$, because it survives the effect which was discussed in the previous paragraph. This is the source S_1 mentioned before in figure 14. The morphology of this source is a hint that it is not part of the *Fermi* Bubbles and therefore, an evidence that the SCA algorithm is not able to filter out only *Fermi* Bubbles to the hard component but also other components. But assuming to know the morphology of the component of interest, this could be used to determine hard contributions which do not belong to this particular component.

The soft component (figure 17 (b)) has nearly no zero pixels but pixels containing many photon counts. This is due to the fact that most sources have an index of $\gamma_s < \gamma$. For example, the brightest pixel has photon counts above 1400 (yellow). If one compares this particular pixel of the soft component map with the same pixel of the hard component map, one can see that this pixel is dark blue, i.e., it has a pixel value of approximately −600 photon counts. The sum of the two components is equal to the modelled data which should be close to the simulated data. Consequently, with this particular index configuration the soft component predicts more photon counts as it should predict. In principle this is not a problem for filtering the hard from the soft contributions, but in this case the hard component looses many photons coming from the *Fermi* Bubbles.

Figure 18 shows the residuals in each pixel integrated over the SCA energy range using $\gamma_h = 2.0$ and $\gamma_s = 2.3$. Overall the residuals are mostly positive, i.e., the model underestimates the data in most of the pixels. But except of a few pixels (yellow) the residual map shows no significant structure. The mean residual

$$\bar{r} = \frac{1}{N_{\mathrm{px}}} \sum_i r_i, \tag{13}$$

where N_{px} is the number of pixels i, is around 6 photon counts and the deviation from the simulated data is less than 3%. This deviation is relatively small. Consequently, the SCA run is accepted. But due to the two resulting component maps this configuration of indices is not suited for the rest of the analysis.

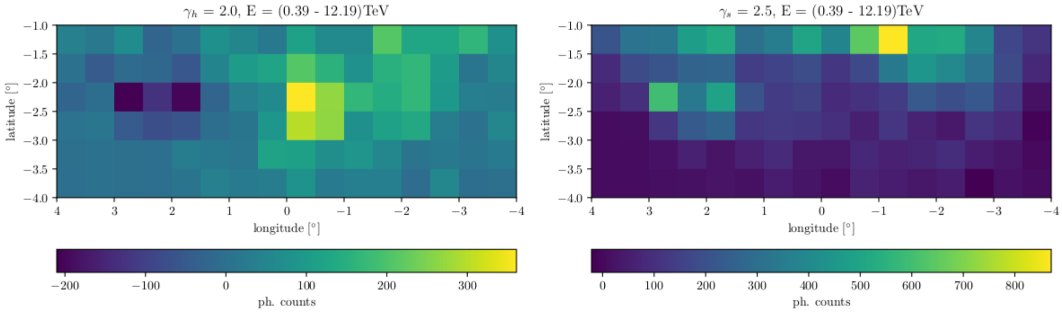

(a) hard component

(b) soft component

Figure 19: The hard and soft component maps of the SCA using the index configuration $\gamma_h = 2.0$ and $\gamma_s = 2.5$. (a) the hard component shows an asymmetry with respect to the vertical axis $l = 0$. Overall there are less negative pixel values. (b) the overestimation of photon counts of the soft component is reduced.

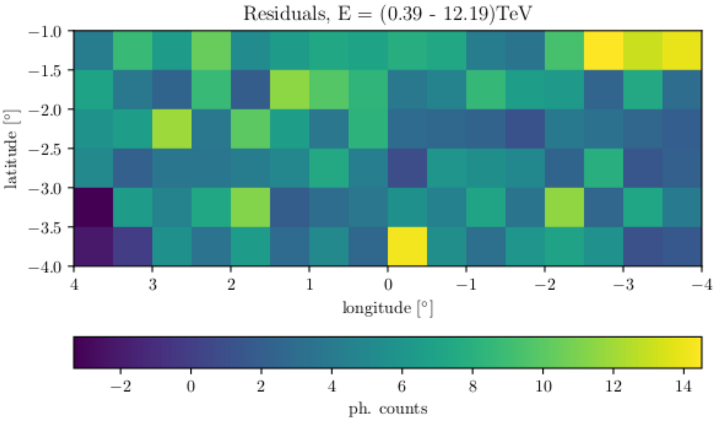

Figure 20: Residuals in each pixel integrated over the energy range used in the SCA. The index configuration is $\gamma_h = 2.0$ and $\gamma_s = 2.5$. Except of some outstanding pixels (yellow) the residual map has smaller residuals compared to figure 18. The mean residual is 5 photon counts. The maximum deviation (yellow) from the simulated data is around 3%.

Figure 19 shows a SCA run using a soft component with an index of $\gamma_s = 2.5$. Compared to the index configuration before, the hard component map (figure 19 (a)) has less pixels with negative photon counts (dark blue). Furthermore, the negative pixel values are larger, i.e., the absolute value in these pixels is smaller for the new index configuration. Hence, it is expected that the overestimation of the soft component (figure 19 (b)) is reduced. If one considers the brightest pixel in the soft component map with around 850 photon counts (yellow), the corresponding pixel in the hard component map has a few tens of photon counts. Thus, the overestimation of the soft component is reduced. Looking into the 1DC model definition file, the contribution in this pixels most likely comes from a bright source called HESS J1745-303 with an index of $\gamma_{\mathrm{HESS}} = 2.7$. As a result of $\gamma_s < \gamma_{\mathrm{HESS}}$ this source should be absorbed by the soft component. Therefore, this pixel is expected to be dominated by HESS J1745-303. On the one hand the soft component contains still more photon counts as expected in some pixels, because there are still negative photon counts in the hard component. But on the other hand, the hard component map seems to estimate the hard contributions in the on-region quite well.

In addition, the hard component map in figure 19 (a) shows an asymmetry with respect to $l = 0$. Neglecting the source S_1 and assuming the morphology of the low-latitude *Fermi* Bubbles in figure 10 (b) this asymmetry indicates the *Fermi* Bubbles. Figure 20 shows the residuals of the SCA run using $\gamma_h = 2.0$ and $\gamma_s = 2.5$. Overall the residuals are positive, i.e., the model underestimates the data again. But except of some outstanding pixels (yellow) the residual map has smaller residuals compared to the previous index configuration and show no significant structure. The mean residual is 5 photon counts and the deviation from the simulated data is less than 3%. The quality of the SCA run is therefore quite good.

Figure 21 shows the last index configuration which will be discussed here. The hard component index is still $\gamma_h = 2.0$ and the soft component index is set to $\gamma_s = 2.7$. Again the number of negative pixels in the hard component map (figure 21 (a)) is reduced compared to the two previous scenarios. This is a consequence of the larger difference between the two SCA input parameters γ_h and γ_s. The photon counts of the soft component (figure 21 (b)) is reduced further. But now it is more likely to get more contributions from soft components to the hard component map, because the range of the intermediate index is larger compared to the index configurations considered before. That means more contributions on top of the *Fermi* Bubbles are expected. This would lead to a misleading larger signal of the *Fermi* Bubbles. For instance, the hard component map has probably some contribution from the source HESS J1745-303 mentioned above. If one compares the bright pixel (yellow) in the soft component map of figure 21 (b) with the corresponding pixel in the hard component map of figure 21 (a), the photon counts of the hard component is increased there compared to the previous scenarios.

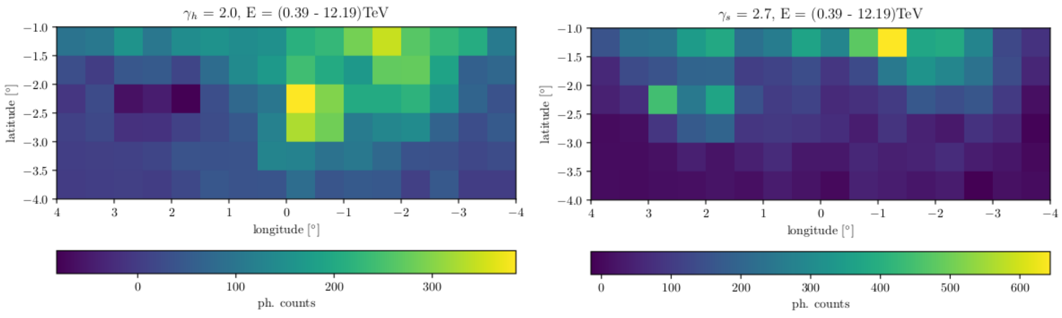

(a) hard component

(b) soft component

Figure 21: The hard and soft component maps of the SCA using the index configuration $\gamma_h = 2.0$ and $\gamma_s = 2.7$. (a) the hard component map has only a few negative pixels. But because of some softer contributions to the hard component the signal of the *Fermi* Bubbles could be larger misleadingly. (b) the soft component map is still brighter than the hard component.

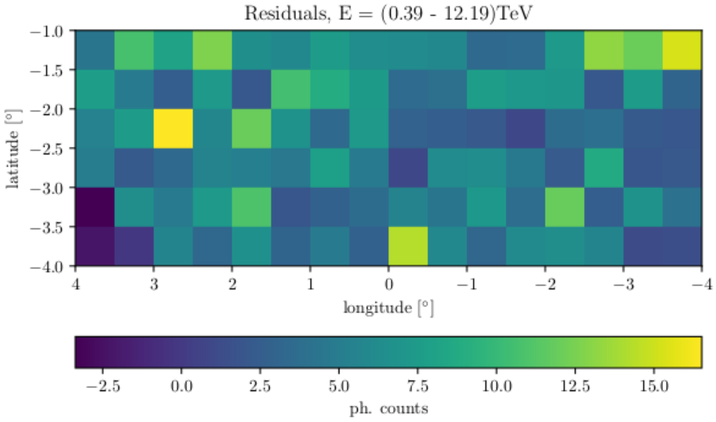

Figure 22: Residuals in each pixel integrated over the energy range used in the SCA with the index configuration of $\gamma_h = 2.0$ and $\gamma_s = 2.7$. Except of a few pixels (yellow) the residual map has low residuals. The mean residual is 6 photon counts. The maximum deviation from the simulated data (yellow) is around 4%.

The residuals of this index configuration (figure 22) are positive and except of a few pixels (yellow) it shows no significant structure again. The mean residual is around 6 photon counts. The deviation from the simulated data is less than 4%. Therefore, the SCA run is accepted, but the index configuration is not suited for further analysis steps.
In principle the hard component index could also be changed, for example to a harder index of $\gamma_h = 1.8$. But reducing the SCA input parameter of the hard component would also mean that the component of interest becomes a source with an intermediate index and therefore contributing to both SCA components. The *Fermi* Bubbles contribution to the hard component would decrease. Increasing the hard component index from $\gamma_h = 2.0$ to, e.g., $\gamma_h = 2.2$ would, on the one hand, result in a hard component map which probably absorbs the *Fermi* Bubbles, but on the other hand in a hard component map with more soft contributions. Therefore, the overall brightness of the hard component would be increased. Consequently, the signal of the *Fermi* Bubbles would be overestimated.
To summarize the observations of different index configurations one can say that the SCA works similar for all three index configurations. There is no index configuration which can be used to filter the *Fermi* Bubbles out from the data perfectly. Different configurations can be used for different purposes. For instance, an index configuration where the soft index is close to the hard index reveals hard background sources in the hard component map. The index configuration used for the following analysis is a hard component index of $\gamma_h = 2.0$ and a soft component index of $\gamma_s = 2.5$ shown in figure 19. It is recommended to test the chosen index configuration on simulations before applying the SCA to real data.
The SCA could be applied to the same data but in a different energy range. At higher energies, e.g., above 10 TeV, there are less photon counts in each pixel due to a lower flux and the number of zero pixels increases (figure 16). Consequently, the pixel size has to be enlarged again loosing spatial resolution. It is recommended to apply the SCA to an energy range where the number of photons is large and the number of zero pixels is small. As mentioned above the SCA works best if

the spectral form is different. Therefore, it is possible to choose a certain energy range where one expects a maximal difference in the spectra.

Regarding the on-off analysis which will be applied to the hard component map to detect the signal from the *Fermi* Bubbles, negative photon counts in the hard component map will be set to zero. This reduces the influence of these pixels to the next analysis steps. More information about the on-off analysis is given in the next section.

5.3 On-Off Analysis

Having the two component maps from the SCA, the focus is now on the hard component map of figure 19 (a), but prepared for the on-off analysis, i.e., all negative pixel values are set to zero. Furthermore, it is assumed that the photon counts originate mostly from the *Fermi* Bubbles, neglecting the source S_1.

The on-off analysis itself is a simple analysis, using the defined on- and off-regions in section 5.1 and their on- and off-pixels (figure 12). The way this analysis works is to subtract the off-region from the on-region. In other words subtracting the off-counts in each off-pixel from the corresponding on-counts in each on-pixel. Because of the asymmetry of the southern low-latitude *Fermi* Bubbles, the difference between the on- and off-pixels can be considered as the detected *Fermi* Bubbles signal in each on-pixel S_j, where

$$S_j = N_j - N_{-j}. \tag{14}$$

The N_j denotes the on-counts in the on-pixel j, whereas N_{-j} denotes the off-counts in the corresponding off-pixel $-j$. The statistical error of S_j is given by

$$\Delta S_j = \sqrt{\sigma_j^2 + \sigma_{-j}^2}, \tag{15}$$

where σ_j^2 and σ_{-j}^2 is the variance of the SCA in the on- and off-pixel, respectively. For further reading see Appendix B. Assuming the remaining background in the hard component map, i.e., all remaining source contributions which do not come from the *Fermi* Bubbles, is symmetric to the vertical axis $l = 0$, the difference S_j is the signal of the *Fermi* Bubbles.

Figure 23 shows the result of the on-off analysis applied to the hard component map. The ROI is divided into different b-bands with a band width of $\Delta b = 0.5°$. The dashed lines represents the expected signal from the *Fermi* Bubbles and therefore, they show the expected longitude profile in each b-band. The expected signal is defined by

$$S_j^{\mathrm{E}} = m_j^{\mathrm{FB}} - m_{-j}^{\mathrm{FB}}, \tag{16}$$

where $m_j^{\mathrm{FB}} = \sum_{i \in j} m_i^{\mathrm{FB}}$ are the expected photon counts of the *Fermi* Bubbles in an on- or off-pixel. Whereas the points are the measured signal S_j in an on-pixel within the considered b-band.

The longitude profiles can be reproduced within the statistical error in most of the b-bands. But there are some signal values which are lower or higher as the expected signal. This is because of the fact that the symmetric background assumption holds not for all on-pixels. On the one hand this leads to negative signals if $N_j < N_{-j}$, i.e., the off-pixel is dominated by a background source. On the other hand this leads to larger signals as expected if $N_j > N_{-j}$, i.e., the on-pixel is dominated by a background source. The latter case can be seen in figure 23 within the longitude of $-1 < l < 0$ and two b-band, namely the band from $-3 < b < -2.5$ (blue) and from $-2.5 < b < -2$ (light blue). These measured signals are at least a factor of two larger than the expected signal from the *Fermi* Bubbles and are correlated with the source S_1, as noticed already in section 5.2.1. Therefore, these particular on-pixels of these two b-bands will be neglected for further analysis steps.

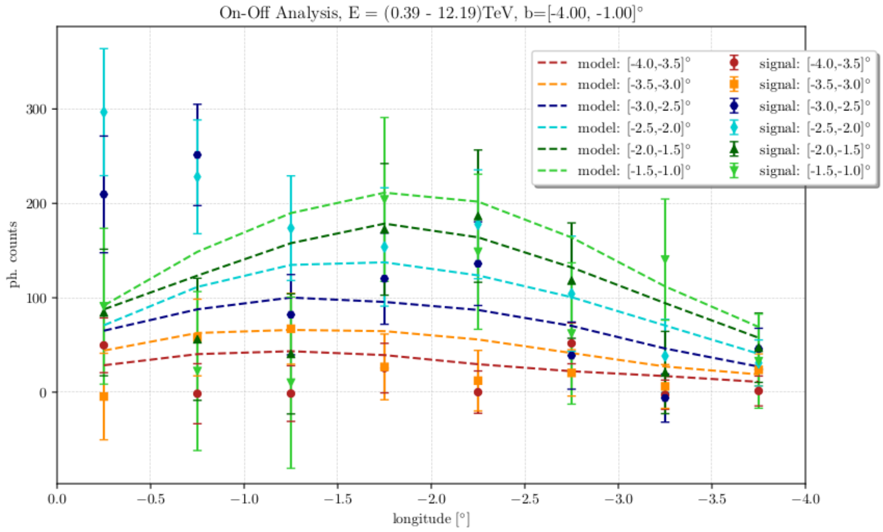

Figure 23: Results of the on-off analysis (points) applied to the hard component of figure 19. The ROI is divided into different latitude bands with a band width of $\Delta b = 0.5°$. In each latitude band the on-off analysis is applied. The expected longitude profile of the *Fermi* Bubbles (dashed lines) can be reproduced whithin the statistical error in most latitude bands and on-pixels. There are some outstanding signals in the latitude bands of $-3 < b < -2.5$ (blue) and $-2.5 < b < -2$ (light blue) within a longitude of $-1 < l < 0$. Here the signal is at least a factor of two larger than expected. This feature corresponds to the hard background source S_1.

The measured signal from the *Fermi* Bubbles in each b-band and on-pixel can be used to define a new *Fermi* Bubbles template. Based on the hard component map in figure 19 (a), this template is referred to as the output template. The next section deals with how the output template is generated.

5.4 Defining the *Fermi* Bubbles Template

For this purpose some conditions, so called cuts, are introduced to ensure that the measured signal in the previous section comes most likely from the *Fermi* Bubbles. Applying these cuts to the signal, measured in each on-pixel of a certain b-band, and using the hard component map as the basis, leads to the output template. Therefore, this output template finally shows if one can detect the *Fermi* Bubbles or not. The output template is defined in the on-region (see section 5.1).

Due to some background sources which break the assumed symmetry to $l = 0$, the on-off analysis does not work perfectly in each on-pixel. This leads to either larger or lower signals as expected. To avoid this, a trusted signal interval is introduced for each on-pixel (figure 24). The edges $S^{\pm \mathrm{T}}$ of the trusted signal interval for each on-pixel j are defined as follows

$$S_j^{\pm \mathrm{T}} = S_j^{\mathrm{E}} \pm k \cdot \Delta S_j, \tag{17}$$

where S_j^{E} represents the expected signal of the *Fermi* Bubbles in the on-pixel j and $k \in \mathbb{N}$ is the trust factor. The trusted signal interval depends, therefore, on the statistical error of the measured signal. Consequently, all measured signals S_j will be accepted if $S_j^{-\mathrm{T}} \leq S_j \leq S_j^{+\mathrm{T}}$ holds. Otherwise the signal is assumed to be dominated by a background source. In figure 24 these trusted signal intervals are shown together with the expected longitude profile in each b-band. The trust factor is set to $k = 1$.

One more cut is applied to the remaining signals. Signals passing the trusted signal interval should also overcome a certain threshold of the statistical significance. This threshold is defined by

$$\Lambda \leq \frac{S_j}{\Delta S_j}. \tag{18}$$

Applying this threshold to the remaining signals, selects those which can be considered as a significant detection of the *Fermi* Bubbles. A lower threshold would probably lead to a better detection of the *Fermi* Bubbles with respect to the morphology. Whereas a higher threshold could be used to detect the most significant *Fermi* Bubbles signals to measure the spectrum in future analysis.

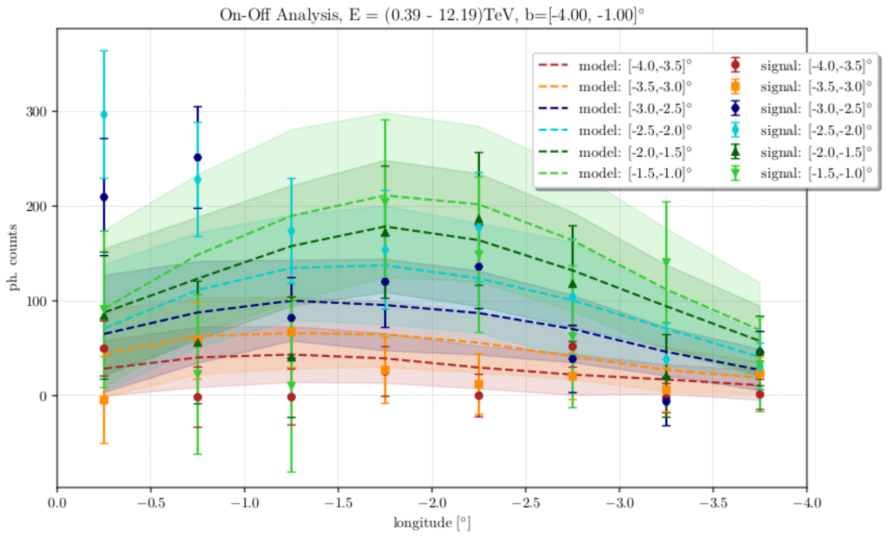

Figure 24: On-off analysis and the trusted signal intervals used to create the output template. The trusted signal interval with the trust factor $k = 1$ is plotted for each latitude band (color coded). Each signal within the trusted signal interval is accepted. Signals outside the trusted signal interval are considered as background dominated.

Figure 25 shows the statistical significance of the remaining signals for $\Lambda = 1$. This is a low threshold to investigate the morphology of the *Fermi* Bubbles in the on-region. The significance of a signal, not passing the trusted signal interval, is set to -1. Therefore, signals which did not pass the trusted signal interval can be seen in figure 25 immediately. Indeed, some signals pass the trusted signal interval but do not overcome the threshold for the statistical significance. Signals with a significance larger than the threshold will contribute to the output template.

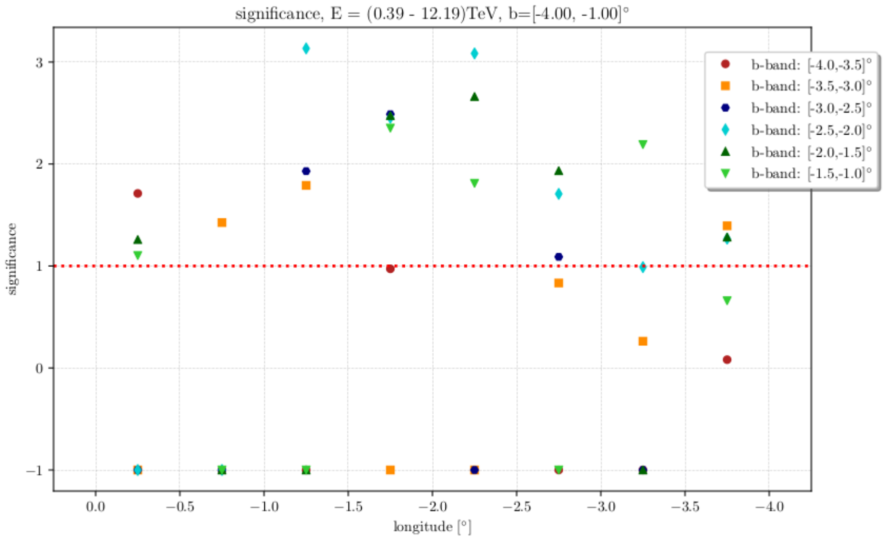

Figure 25: Statistical significance of all signals passing the trusted signal interval. The significance of signals not passing this cut are set to -1. The threshold for the statistical significance is $\Lambda = 1$. This low threshold is chosen to study the morphology of the *Fermi* Bubbles in the on-region.

Applying these two cuts after each other, will result in the most reliable signals from the *Fermi* Bubbles detected in each on-pixel and b-band. The last step of defining the output template is to match all signals to the corresponding on-pixel of the output template. The output template is normalized to the maximum signal $S_{\max}$ and therefore, the maximum entry is one. This normalization is just for comparison of the input and output template and has no influence on the analysis. The result of the output template is shown in figure 26 (b). To investigate the morphology of the low-latitude *Fermi* Bubbles, the output template will be compared to the input template in the same on-region. For this purpose the input template is normalized in the same way as the output template. The two templates can be seen in figure 26. The morphology of the *Fermi* Bubbles can already be estimated by eye. Bright regions in the input template are also bright regions in the output template and vice versa.
But to compare it more quantitatively, the residual

$$r_j = \frac{O_j - I_j}{I_j} \tag{19}$$

is considered. O_j denotes the output template value in the output template pixel j and I_j represents the input template value in the corresponding input template pixel. The result is shown in figure 27. Negative values indicate an underestimation whereas positive values indicate an overestimation of the *Fermi* Bubbles.

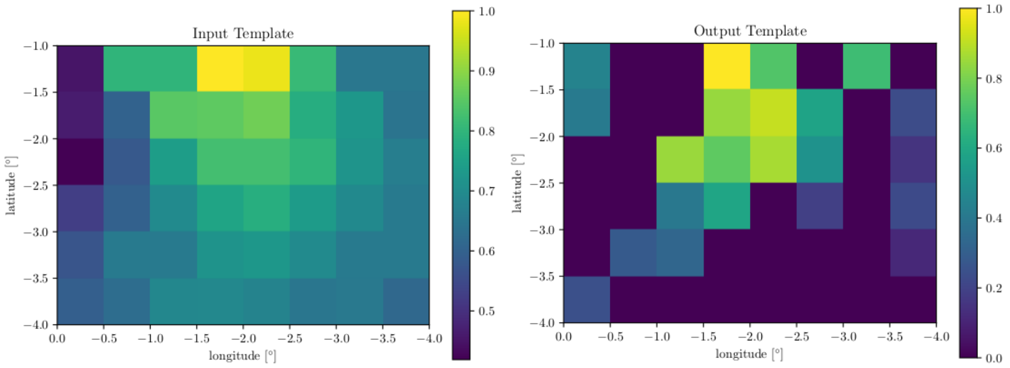

(a) input template

(b) output template

Figure 26: The input (a) and output (b) template. Both are normalized to its maximum pixel value. Bright regions in the input template are also bright regions in the output template.

In comparison with the input template, the output template overestimates the *Fermi* Bubbles in some pixels (yellow). This means there is still some contribution from other sources in the hard component which are not filtered out during this analysis. Some regions are underestimated (blue). This could be due to the SCA, matching some photons of the *Fermi* Bubbles to the soft component. Another reason could be that the *Fermi* Bubbles are not zero in the off-region (figure 10 (b) or figure 13) which will be subtracted from the on-region *Fermi* Bubbles by applying the on-off analysis to the hard component map.

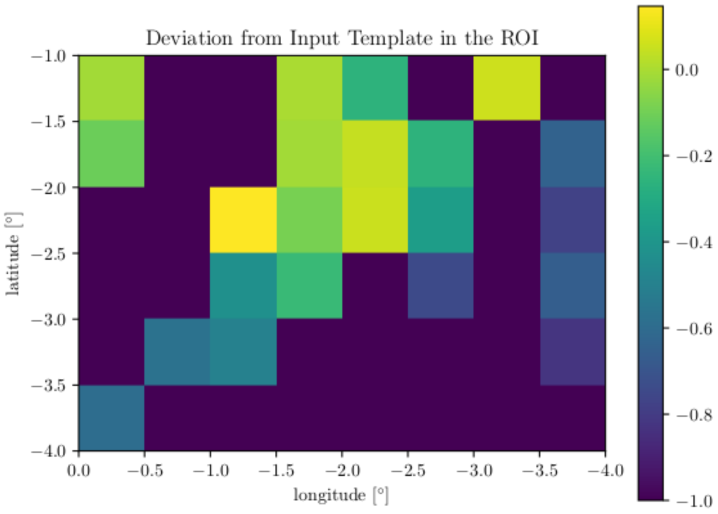

Figure 27: Deviation of the output template from the input template. (green) regions where the output template fits best to the input tamplate. (yellow) regions where the output template overestimates the signal from the *Fermi* Bubbles. (blue) are underestimated regions. Pixel values of −1 indicate that there are no *Fermi* Bubbles detected in this on-pixel.

One can reduce these regions by increasing the threshold, e.g., to $\Lambda = 2$. Furthermore, the ROI can be restricted to $-3 < l < 3$ in longitude and $-2 < b < -1$ in latitude. Applying the on-off analysis to the new ROI with the same parameters as before (figure 28 (a)), calculating the statistical significance (figure 28 (b)) and matching the remaining signals to the corresponding output template pixels again, lead to the new output template in figure 29 (b).

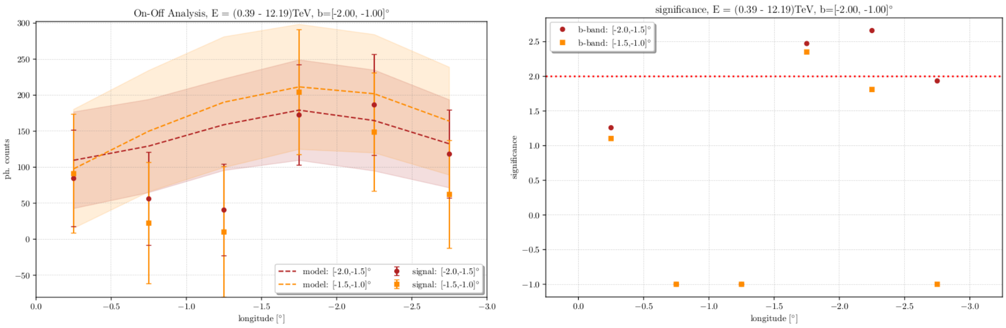

(a) on-off analysis

(b) statistical significance

Figure 28: Results of the on-off analysis (a) and the statistical significance (b) for the new ROI. The trust factor is $k = 1$ again. The threshold for the statistical significance is set to $\Lambda = 2$. In both latitude bands there are underestimated signals which do not pass the trusted signal interval. Increasing the threshold Λ further would lead to a no-detection of the *Fermi* Bubbles.

In figure 28 (a) there are two signals not passing the trusted signal interval in each b-band in the same on-pixel. Therefore, the contribution of the *Fermi* Bubbles is underestimated or the corresponding off-pixels are dominated by a background contribution to the hard component. The signals passing the trusted signal interval overcome the $\Lambda = 2$ threshold (figure 28 (b)). Increasing the threshold further to $\Lambda = 3$ would lead to no *Fermi* Bubbles detection. If one compares the two templates in figure 29 in the same way like before, the underestimated regions are reduced drastically (figure 30). The deviation of the output template from the input template is close to zero in each pixel. Therefore, this is a good detection of the *Fermi* Bubbles.

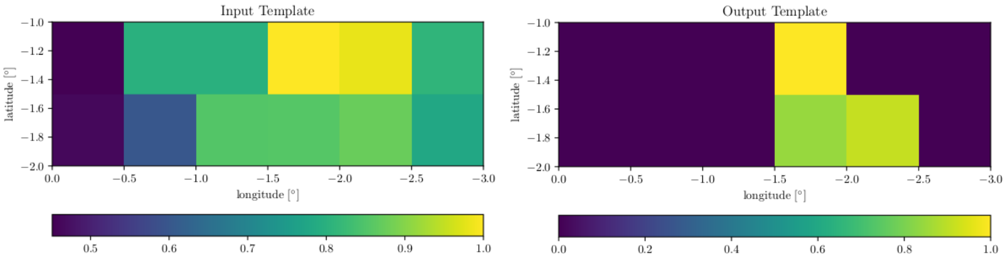

(a) input template

(b) output template

Figure 29: The input (a) and output (b) template for $\Lambda = 2$. The number of output template pixels are reduced to only three remaining pixels in the new ROI.

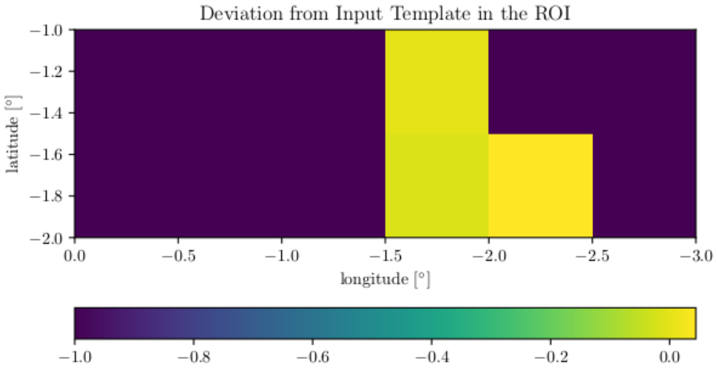

Figure 30: Deviation of the output template from the input template for the new ROI. Running the analysis in this new ROI with the new threshold, reduces the regions of underestimated *Fermi* Bubbles. The deviation is close to zero in each pixel.

Until now, data without the CR background are studied (GCNB-simulation). With this data, one can show that the presented analysis can be used to detect the low-latitude *Fermi* Bubbles at negative latitudes if the data set is cleaned from CR background. The next question is: Will this analysis detect a signal from the *Fermi* Bubbles if no *Fermi* Bubbles are in the simulated data? To show that this is not the case, one can apply the whole analysis to the GCNF-simulation of 50 h (table 1). The cuts and the ROI are the same as in figure 28. The result is shown in figure 31.

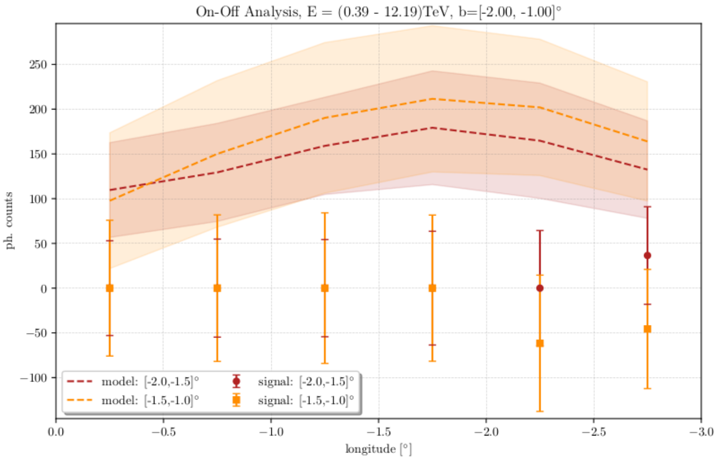

Figure 31: Result of the on-off analysis which is applied to the 50 h GCNF-simulation. All signals do not pass the trusted signal interval and therefore, no signal from the *Fermi* Bubbles is detected.

All signals do not pass the trusted signal interval and therefore, the statistical significance in each on-pixel is set to -1. This means there is no remaining signal from the *Fermi* Bubbles. Consequently, there is no output template generated in this scenario.

5.5 Analysis of a more realistic Scenario

In this section the CR background is added to the simulated data. That means the 50 h GCFB-simulation (figure 32 (a)) is analysed in the following. Using the presented analysis to study the *Fermi* Bubbles with this data set requires a new strategy to estimate the CR background. A possible strategy could be to estimate the CR background by a background observation. This background observation should have the same conditions like the actual observation, e.g., time of observation or the pointing of the telescopes. But it should observe a different region where: The *Fermi* Bubbles are not present and the gamma-ray background is relatively low. Another approach is that other CTA observations are maybe suited to estimate the CR background. Having this in mind one can also think about using CTA sub-arrays (see chapter 2.3). In any case the CR background is estimated by an additional observation. This background observation is simulated in figure 32 (b). The conditions are the same like in the GCFB-simulation. The model used to simulate the CR background is the IRFbackground model for *ctools* shipped with the 1DC.

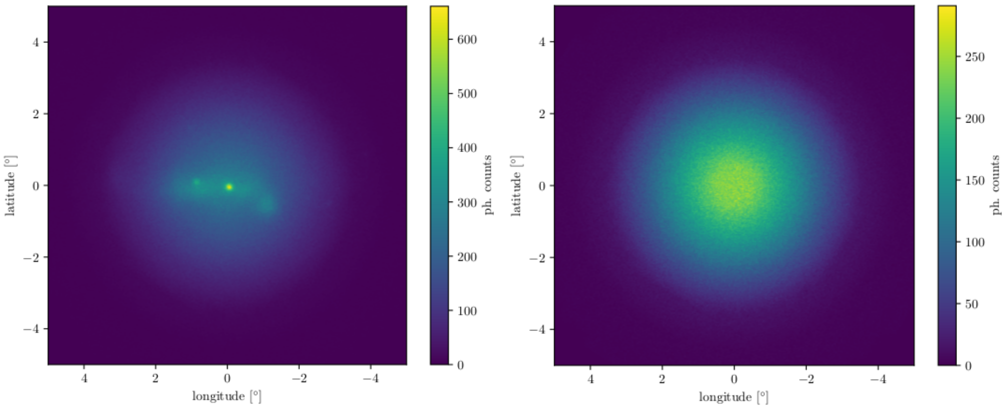

(a) GCFB-simulation (b) BKG-simulation

Figure 32: A more realistic simulation of the GC. (a) the GCFB-simulation (b) the BKG-simulation to estimate the CR background of the GCFB-simulation, including the CR background.

The data set of figure 32 (a) is cleaned by subtracting the estimated CR background of figure 32 (b). The SCA parameters are $\gamma_h = 1.9$, $\gamma_s = 2.5$, $\text{pxs} = 0.5°$ and the energy range is set from 0.39 TeV to 12.19 TeV. The only parameter which has changed is the index of the hard component.

Applying the on-off analysis to the hard component map for the same ROI like before and applying the established cuts to the measured signals lead to the results shown in figure 33 and figure 34. The trust factor is set to $k = 1$ and the threshold of the statistical significance is set to $\Lambda = 1.5$. The measured signals in figure 33 (a) fluctuates more than in previous studies. This can be explained by an increased Poisson noise due to the subtraction of the BKG-simulation. The significance (figure 33 (b)) is lower compared to figure 28 (b) because of subtracting the BKG-simulation from the simulated data. The resulting Poisson noise leads to larger statistical errors of the SCA components. Consequently, the error of the measured signals, passing the trusted signal interval, is increased.

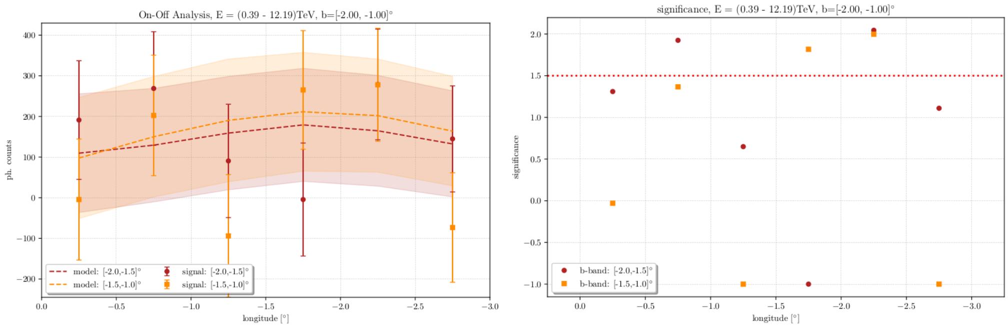

(a) on-off analysis (b) statistical significance

Figure 33: The on-off analysis (a) with more fluctuating measured signals than before. The statistical significance in each on-pixel (b) is reduced because of larger statistical errors of the signals.

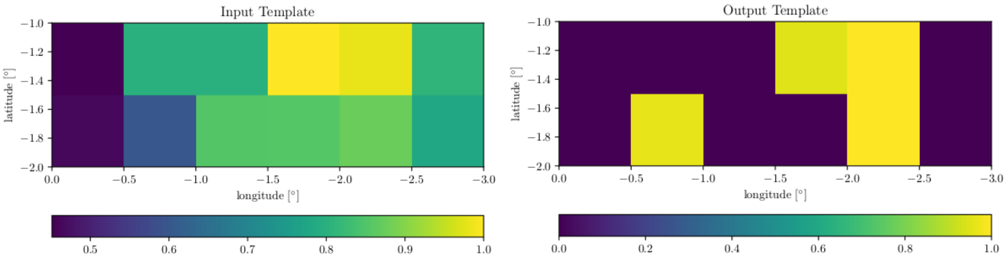

(a) input template (b) output template

Figure 34: The input template (a) and the output template (b). These templates are the result of analysing the data from the GCFB-simulation.

Finally, the output template (figure 34 (b)) is generated and can be compared to the input template (figure 34 (a)). The result is shown in figure 35. The analysis with the parameters above tend to overestimate the *Fermi* Bubbles. This is shown by green and yellow regions in figure 35. Consequently, there are more soft components contributing to the hard component map. These contributions most likely come from the CR background, especially in the yellow region. Nevertheless, with a data set including a more general background it is possible to detect the *Fermi* Bubbles with the presented analysis strategy in chapter 5. The blue regions, seen in figure 35, are close to zero. That means the signal from the *Fermi* Bubbles are close to the expected one.

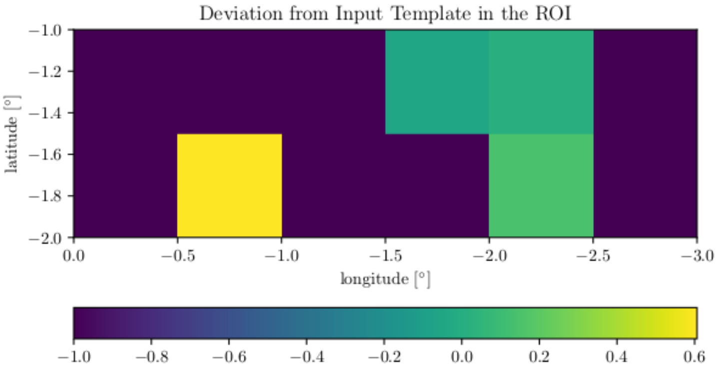

Figure 35: Deviation of the output template from the input template. The output template tend to overestimate the *Fermi* Bubbles.

6 Conclusion and Outlook

In this work an analysis strategy is presented to detect the souther low-latitude *Fermi* Bubbles with CTA. For this analysis the extended source sensitivity of CTA is estimated. This estimation shows that CTA will be sensitive to the *Fermi* Bubbles for observation times larger than 5 h. With the introduced analysis it is nearly impossible to detect the *Fermi* Bubbles in a more realistic 5 h observation, but Appendix C shows the analysis applied on the GCNB-simulation of 5 h. CTA will therefore be the first ground based gamma-ray telescope which will be able to detect the *Fermi* Bubbles. Furthermore, an analysis chain is developed to detect the southern low-latitude *Fermi* Bubbles. Choosing only low latitudes is reasonable because of three basic facts: The low-latitude *Fermi* Bubbles have a significantly harder spectrum like the *Fermi* Bubbles at higher latitudes. In addition, the *Fermi* Bubbles are brighter at low latitudes and the ROI can be smaller due to the morphology of the low-latitude *Fermi* Bubbles. Finally, the southern low-latitude *Fermi* Bubbles reveal an asymmetry with respect to the vertical axis $l = 0$. These basics can be used to detect the *Fermi* Bubbles at low latitudes.

The first analysis step is to distinguish the *Fermi* Bubbles from other sources. For this purpose the SCA is applied to the data in a certain ROI. This analysis takes advantage of the harder spectrum and is a semi-blind analysis. The results of this analysis step are two count maps representing the filtered *Fermi* Bubbles and all the other source components, respectively. But the SCA has some problems: The outcome of the SCA is highly dependent on the input parameters, namely the spectral form of the spectral components. Therefore, one has to assume the spectral form and the spectral index of the desired component. In addition, the SCA is not able to distinguish the *Fermi* Bubbles from other components perfectly. Consequently, in the component which represents the *Fermi* Bubbles are still contributions from other sources. In the future, this problem can be solved by improving the understanding of the gamma-ray background in the vicinity of the GC. Well modelled sources can than be subtracted from the data. Because of a great exposure of around 300 h of the inner 10° of our galaxy, CTA will also contribute to this improvement for sure. Another aspect is that the SCA does not work for pixels with zero photon counts. This problem appears especially for very low and very high energies. One easy solution is to increase the pixel size of a single pixel. But the spatial resolution decreases with increasing pixel size. Therefore, a proper compromise between the number of zero pixels and the spatial resolution has to be found. The better solution is to restrict the SCA to the ROI. In this case, the problem of zero pixels should be solved for low energies and therefore, the remaining zero pixels are expected at higher energies. Choosing the proper energy range for the SCA will than lead to no zero pixels. If this is not enough, a smoothing can be applied to the data. Zero pixels will therefore get some contributions from the neighbouring pixels. It is recommended to test the SCA on a suited simulation before applying it to real data.

In the next analysis step the asymmetry of the southern low-latitude *Fermi* Bubbles is used to detect a *Fermi* Bubbles signal. The way this analysis step works is an on-off analysis. This analysis assumes a symmetric background with respect to the vertical axis $l = 0$. Therefore, the on-off analysis suffers because of background sources breaking the assumed symmetry. As a result the on-off analysis might overestimate the signal, if the background source is on top of the *Fermi* Bubbles. If the background source is complementary to the *Fermi* Bubbles, i.e., where no *Fermi* Bubbles are expected, the on-off analysis can underestimate the signal. Improving the outcome of the SCA such that the assumption of a symmetric background holds, improves therefore the result of the on-off analysis. The final analysis step is to apply some conditions to the signals. Signals satisfying these conditions are considered as signals coming from the *Fermi* Bubbles. On the one hand each signal has to pass a trusted signal interval. This condition ensures to take only signals into account which are in the same order as the expected signals from the *Fermi* Bubbles. On the other hand the statistical significance of the signals, surviving the first condition, has to overcome a certain threshold. This is also to quantify the quality of the detection. All surviving signals take part to define an output template of the *Fermi* Bubbles. The overall exposure of around 300 h of the GC region will improve the significance of the detection, because only 50 h are considered in this work. The *Fermi* Bubbles can already be detected.

In the future CTA will not only detect a signal from the *Fermi* Bubbles, furthermore it is crucial to investigate the spectrum of the *Fermi* Bubbles at energies above 1 TeV. At these energies the *Fermi*-LAT loses sensitivity. The current data from the *Fermi* Bubbles, therefore, are below 1 TeV. To confirm the observation of a harder spectrum at low latitudes, it is essential to reconstruct the spectrum of the low-latitude *Fermi* Bubbles with CTA above 1 TeV. For this purpose the output templates, generated as a result of the presented analysis chain, can be used by *ctools* for example.

The results of this work are achieved with simulated data of only 50 h observations. Compared to the exposure of 300 h of the inner regions of our galaxy, including the regions discussed here, the overall exposure is six times larger. Consequently, one can expect great results of CTA observing the *Fermi* Bubbles regarding the morphology, investigating the base and therefore the origin, and the spectrum above 1 TeV. Moreover CTA will hopefully rule out the origin of the *Fermi* Bubbles.

Appendix

Appendix A: Estimate the extended Source Sensitivity

To estimate the sensitivity of CTA to an extended source, based on the point source sensitivity, the field of view is divided into two regions. The on-region Ω_{ON} is defined as the region where the extended source is located within the field of view. The background region Ω_{BKG}, also referred to as the off-region, is defined as the remaining area of the field of view. If one considers the extended source as a certain number of point sources n_{ps}, the extended source sensitivity can be estimated based on the point source sensitivity.
The point source sensitivity shown in section 2.3 is defined as the flux F coming from the source of interest needed to detect this source with a statistical significance of 5σ. The extended source sensitivity is defined in the same way. Consequently, the statistical significance for the extended source should be equal to the statistical significance of a point source. The statistical significance σ is given by

$$\sigma_i = \frac{N_i}{\sqrt{N_i^{\mathrm{bkg}}}}, \tag{20}$$

where N_i are the total photon counts detected in a point-like ($i = \mathrm{ps}$) or in an extended-like ($i = \mathrm{ext}$) scenario, respectively. N_i^{bkg} denotes the photon counts of the background for each scenario. In the extended-like scenario the background counts can be estimated via the point spread function, which describes the response of an imaging instrument to a point source. The background counts $N_{\mathrm{ext}}^{\mathrm{bkg}}$ is given by

$$N_{\mathrm{ext}}^{\mathrm{bkg}} = N_{\mathrm{ps}}^{\mathrm{bkg}} \cdot n_{\mathrm{ps}} = N_{\mathrm{ps}}^{\mathrm{bkg}} \cdot \frac{\Omega_{\mathrm{ON}}}{\Omega_{\mathrm{PSF}}}, \tag{21}$$

where Ω_{PSF} is the size of the point spread function. Using $\sigma_{\mathrm{ext}} = \sigma_{\mathrm{ps}}$ to get N_{ext}, the detected flux F_{ext} of an extended source can be estimated via

$$F_{\mathrm{ext}} = \frac{N_{\mathrm{ext}}}{A_{\mathrm{eff}}T} = \frac{N_{\mathrm{ps}} \cdot \sqrt{\frac{\Omega_{\mathrm{ON}}}{\Omega_{\mathrm{PSF}}}}}{A_{\mathrm{eff}}T} = F_{\mathrm{ps}} \cdot \sqrt{\frac{\Omega_{\mathrm{ON}}}{\Omega_{\mathrm{PSF}}}} \tag{22}$$

The sensitivity shown in section 3.3 is normalized to the region of interest to compare it to the data in Ackermann, Ajello, et al. 2017. The sensitivity is therefore

$$I_{\mathrm{ext}} = \frac{F_{\mathrm{ext}}}{\Omega_{\mathrm{ON}}} = \frac{F_{\mathrm{ps}}}{\sqrt{\Omega_{\mathrm{PSF}} \cdot \Omega_{\mathrm{ON}}}}. \tag{23}$$

The estimated extended source sensitivity shown in figure 9 is calculated with a field of view of a radius $R_{\mathrm{FOV}} = 5°$. The radius of the point spread function is assumed to be $R_{\mathrm{PSF}} = 0.05°$. Furthermore, the region of interest is set to the half of the field of view. The data used for the point source sensitivity are the same as shown in figure 5.

Appendix B: Spectral Component Analysis

In general more than two components of the diffuse emission process can be considered by the spectral component analysis. Therefore, a more general way to describe the SCA using the χ^2 data analysis principle is shown below. This description follows in principle the one given in Malyshev 2012.

The SCA assumes energy spectra with a functional form $f_{i\nu\alpha}$. This functional form depends on the pixel index i, the component ν and the energy α. The data $d_{i\alpha}$ can be written as

$$d_{i\alpha} = \sum_{\nu} T_{i\nu} f_{i\nu\alpha}, \tag{24}$$

where $T_{i\nu}$ are the normalization factors for each component, assuming that it is independent of the energy. Minimizing the χ^2

$$\chi^2 = \sum_{\alpha} \sum_{i} \frac{(d_{i\alpha} - \sum_{\nu} T_{i\nu} f_{i\nu\alpha})^2}{\sigma_{i\alpha}^2}, \tag{25}$$

respect to $T_{i\nu}$ lead to

$$\sum_{\alpha} \frac{d_{i\alpha} f_{i\nu\alpha}}{\sigma_{i\alpha}^2} = \sum_{\nu'} T_{i\nu'} \sum_{\alpha} \frac{f_{i\nu'\alpha} f_{i\nu\alpha}}{\sigma_{i\alpha}^2}, \tag{26}$$

where $\sigma_{i\alpha}^2$ is the variance. This Equation can be simplified by defining the matrix D as

$$D_{i\nu} = \sum_{\alpha} \frac{d_{i\alpha} f_{i\nu\alpha}}{\sigma_{i\alpha}^2} \tag{27}$$

and the matrix F as

$$F_{i\nu'\nu} = \sum_{\alpha} \frac{f_{i\nu'\alpha} f_{i\nu\alpha}}{\sigma_{i\alpha}^2}, \tag{28}$$

which are both positive matrices. In addition F is a regular matrix. Equation (26) looks therefore like

$$D_{i\nu} = \sum_{\nu'} T_{i\nu'} F_{i\nu'\nu}. \tag{29}$$

The solution of minimizing the χ^2 of equation (25) with respect to $T_{i\nu}$ is given by

$$T_{i\nu} = \sum_{\nu} D_{i\nu} (F_i)^{-1}_{\nu\nu'}. \tag{30}$$

Because of counting single photons, one can presume Poisson statistics. Consequently, the variance $\sigma_{i\alpha}^2$ is equal to the mean value of counted photons in each pixel and energy bin. In this case $\sigma_{i\alpha}^2 = d_{i\alpha}$. Therefore, the SCA is not working in pixels with zero photon counts. Especially for high energies zero photon counts is a sincere problem. The data can be prepared to avoid zero photon counts by enlarge the pixel size and reduce the number of energy bins. If there is still an pixel with zero photon counts, this particular pixel has no information and the SCA will jump over this pixel.

The minimization problem described above is linear in $T_{i\nu}$. The uncertainties can therefore be found by using the Hessian matrix of the problem (Sivia et al. 2006).

It turns out that the Hessian matrix, which is a square matrix of second order partial derivatives

$$\frac{\partial^2 \chi^2}{\partial T_{i\nu} \partial T_{i\nu'}} = (F_i)^{-1}_{\nu\nu'} = \sigma_i^2. \tag{31}$$

Because of the Poisson statistics the variance is additive, i.e., the variance in an on- or off-pixel, used in the on-off analysis later, is

$$\sigma_j^2 = \sum_{i \in j} \sigma_i^2. \tag{32}$$

The uncertainties of $T_{i\nu}$ are given by

$$\sigma_i = \sqrt{(F_i)^{-1}_{\nu\nu'}}. \tag{33}$$

Appendix C: Analysis applied to a 5h Simulation

The *Fermi* Bubbles can also be detect with observations of only 5 h of observation time but with less statistics. Therefore, the pixel size of a single pixel is increased to pxs = 1 deg. The morphology of the *Fermi* Bubbles is hard to detect with this pixel size, but it is possible to detect a signal in some on-pixels. For the analysis of the GCNB-simulation of 5 h the following parameters are used: The hard and soft component index is $\gamma_h = 2.0$ and $\gamma_s = 2.5$, respectively. The energy range for the SCA is defined from 0.39 TeV to 12.19 TeV again. The trust factor is $k = 1$ and the threshold is set to $\Lambda = 1$. The results of the analysis of a simulated 5 h observation is shown in the figures 36 to 40.

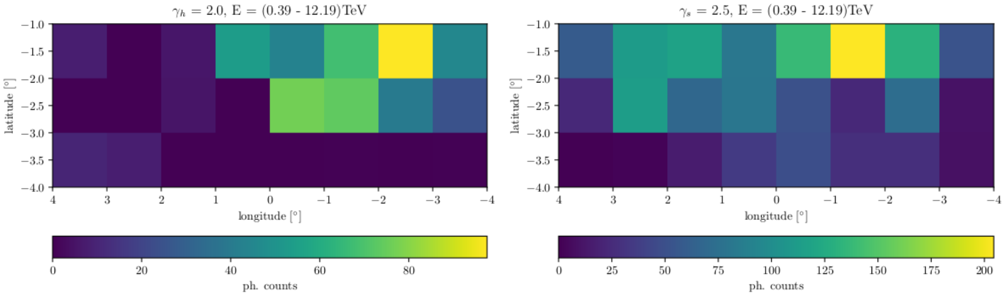

(a) hard component

(b) soft component

Figure 36: (a) the hard component reveals still an asymmetry with respect to the vertical axis $l = 0$. (b) shows the soft component map

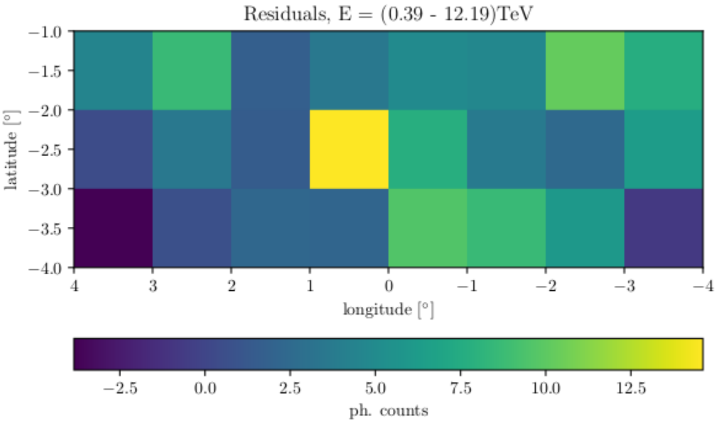

Figure 37: The residual map of the SCA component maps has a mean residual of $\bar{r} = 5$ photon counts. There are some large residuals (green to yellow) with a maximum deviation from the simulated data of around 19% which is quite large.

Overall it is hard to detect the *Fermi* Bubbles in a data set of only 5 h of observation time. Furthermore, the GCNB-simulation is used here. Using a more realistic situation, e.g., the GCFB-simulation, the analysis cannot detect the *Fermi* Bubbles in such a data set. Therefore, a larger exposure is needed. Increasing the exposure time for the *Fermi* Bubbles would lead to a better detection with a higher statistical significance.

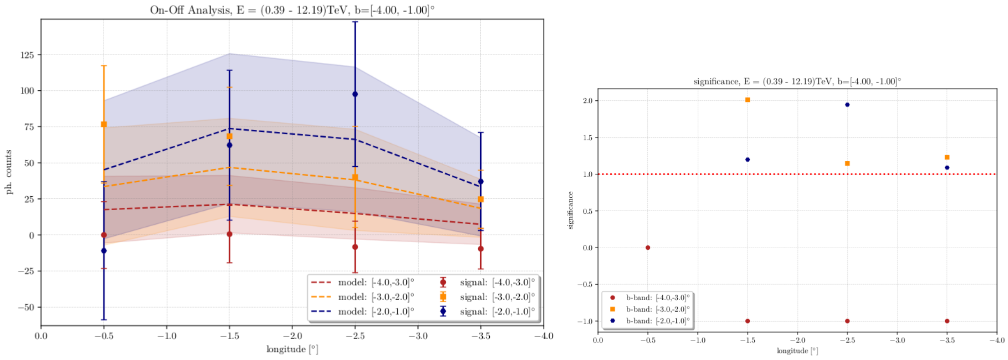

(a) on-off analysis (b) statistical significance

Figure 38: Applied cuts to the hard component map. (a) the on-off analysis is able to reconstruct the expected longitude profil of the *Fermi* Bubbles. Nearly all measured signals lie in between the trusted siganl interval with a trust factor of $k = 1$ but have large errors. (b) the threshold of the statistical significance is set to $\Lambda = 1$. A few signals overcome this threshold and therefore, the *Fermi* Bubbles are detected in these on-pixels.

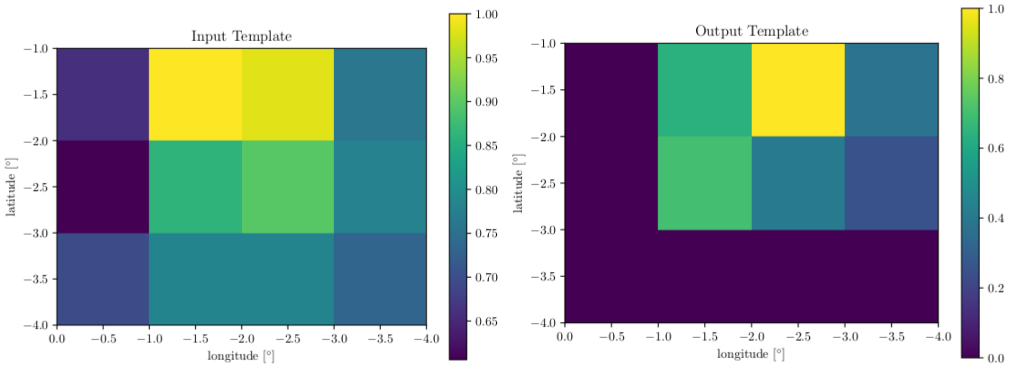

(a) input template (b) output template

Figure 39: The comparison of the input (a) and output template (b). The analysis detects the *Fermi* Bubbles in the brighter regions of th input template.

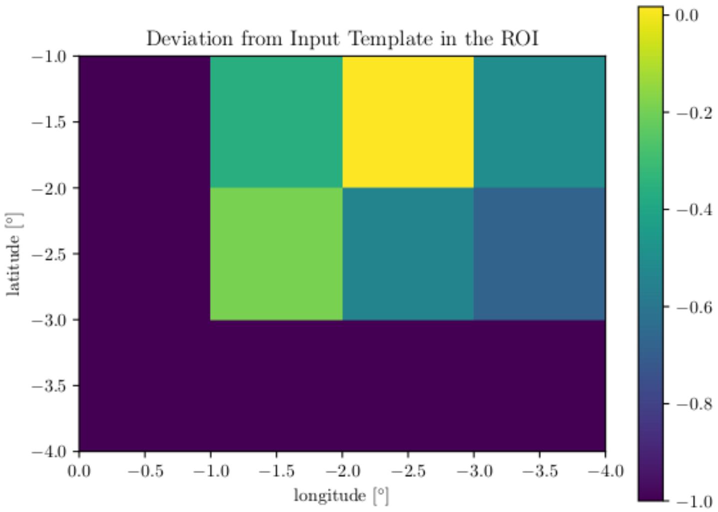

Figure 40: Deviation of the output template from the input template. The output template tend to underestimate the *Fermi* Bubbles in most of the on-pixels (green to blue). Only one on-pixel fits to the corresponding on-pixel of the input template (yellow). This pixel is nearly zero.

List of Figures

Glossary

1DC First CTA Data Challenge.

AGN Active Galactic Nuclei.

b-band latitude band.

BH Black Hole.

BKG Background.

CMB Cosmic Microwave Background.

CR Cosmic Ray.

CTA Cherenkov Telescope Array.

DM Dark Matter.

FB *Fermi* Bubbles.

FOV Field of View.

GC Galactic Center.

GP Galactic Plane.

IACT Imaging Atmospheric Cherenkov Telescope.

IC Inverse Compton.

IEM Interstellar Emission Model.

IRF Instrument Response Function.

ISRF Interstellar Radiation Field.

LAT Large Area Telescope.

LST Large-Sized Telescope.

MST Medium-Sized Telescope.

NS Neutron Star.

PM Photomultiplier.

PSF Point Spread Function.

PWN Pulsar Wind Nebulae.

ROI Region Of Interest.

SCA Spectral Component Analysis.

SMBH Super Massive Black Hole.

SN Supernova.

SNR Supernova Remnant.

SST Small-Sized Telescope.

VHEU Very-High-Energy Universe.

References

Ackermann, M, M Ajello, et al. (2017). "The Fermi Galactic Center GeV excess and implications for dark matter". In: *The Astrophysical Journal*.

Ackermann, M, A Albert, et al. (2014). "The spectrum and morphology of the Fermi bubbles". In: *The Astrophysical Journal*.

Čerenkov, PA (1937). "Visible radiation produced by electrons moving in a medium with velocities exceeding that of light". In: *Physical Review*.

Cheng, K-S, DO Chernyshov, VA Dogiel, C-M Ko, and W-H Ip (2011). "Origin of the Fermi bubble". In: *The Astrophysical Journal Letters*.

Crocker, Roland M and Felix Aharonian (2011). "Fermi bubbles: giant, multibillion-year-old reservoirs of galactic center cosmic rays". In: *Physical Review Letters*.

CTA Consortium, The Cherenkov Telescope Array et al. (2017). "Science with the Cherenkov Telescope Array". In: *arXiv preprint arXiv:1709.07997*.

CTA, Website (March, 2018). URL: `https://www.cta-observatory.org`.

De Angelis, Alessandro and Mário João Martins Pimenta (2015). *Introduction to Particle and Astroparticle Physics: Questions to the Universe*. Springer.

Dobler, Gregory, Douglas P Finkbeiner, Ilias Cholis, Tracy Slatyer, and Neal Weiner (2010). "The Fermi haze: a gamma-ray counterpart to the microwave haze". In: *The Astrophysical Journal*.

ESO, Website (April, 2018). URL: `https://www.eso.org`.

Finkbeiner, Douglas P (2004). "Microwave interstellar medium emission observed by the Wilkinson Microwave Anisotropy Probe". In: *The Astrophysical Journal*.

Fox, Andrew J et al. (2015). "Probing the Fermi Bubbles in Ultraviolet Absorption: A Spectroscopic Signature of the Milky Way's Biconical Nuclear Outflow". In: *The Astrophysical Journal Letters*.

Goodenough, Lisa and Dan Hooper (2009). "Possible evidence for dark matter annihilation in the inner Milky Way from the Fermi Gamma Ray Space Telescope". In: *arXiv preprint arXiv:0910.2998*.

Grupen, Claus (2005). *Astroparticle physics*. Springer Science & Business Media.

IRAP, Website (March, 2018). URL: `http://cta.irap.omp.eu`.

Knödlseder, J et al. (2016). "GammaLib and ctools-A software framework for the analysis of astronomical gamma-ray data". In: *Astronomy & Astrophysics*.

Laing, Robert A, JR Canvin, AH Bridle, and MJ Hardcastle (2006). “A relativistic model of the radio jets in 3C 296”. In: *Monthly Notices of the Royal Astronomical Society*.

Malyshev, Dmitry (2012). “Spectral components analysis of diffuse emission processes”. In: *arXiv preprint arXiv:1202.1034*.

— (2017). “Fermi Bubbles: an elephant in the gamma-ray sky”. In: *EPJ Web of Conferences*.

Mangano, Salvatore (2017). “Cherenkov Telescope Array Status Report”. In: *arXiv preprint arXiv:1705.07805*.

McNamara, BR and PEJ Nulsen (2007). “Heating hot atmospheres with active galactic nuclei”. In: *Annu. Rev. Astron. Astrophys.*

Mertsch, Philipp and Subir Sarkar (2011). “Fermi gamma-ray “bubbles” from stochastic acceleration of electrons”. In: *Physical Review Letters*.

NASA, Website (April, 2018). URL: https://www.nasa.gov.

Paumard, Thibaut et al. (2006). “The two young star disks in the central parsec of the galaxy: properties, dynamics, and formation”. In: *The Astrophysical Journal*.

Sivia, Devinderjit and John Skilling (2006). *Data analysis: a Bayesian tutorial*. OUP Oxford.

Sofue, Yoshiaki and Andreas Vogler (2001). “Bipolar hypershell models of the extended hot interstellar medium in spiral galaxies”. In: *Astronomy & Astrophysics*.

Su, Meng, Tracy R Slatyer, and Douglas P Finkbeiner (2010). “Giant gamma-ray bubbles from Fermi-LAT: AGN Activity or Bipolar Galactic Wind?” In: *The Astrophysical Journal*.

Vitale, Vincenzo, Aldo Morselli, et al. (2009). “Indirect search for dark matter from the center of the milky way with the Fermi-Large Area Telescope”. In: *arXiv preprint arXiv:0912.3828*.

Yang, H-YK, M Ruszkowski, PM Ricker, E Zweibel, and D Lee (2012). “The Fermi Bubbles: Supersonic Active Galactic Nucleus Jets with Anisotropic Cosmic-Ray Diffusion”. In: *The Astrophysical Journal*.

Zubovas, K, AR King, and S Nayakshin (2011). “The Milky Ways Fermi bubbles: echoes of the last quasar outburst?” In: *Monthly Notices of the Royal Astronomical Society: Letters*.

Acknowledgement

I would like to thank Prof. Dr. Stefan Funk for offering this outstanding topic for my Master's Thesis and Dr. Dmitry Malyshev for his patience and not being tiered to explaining things. I also want to thank the whole gamma group for the warm welcome, especially to mention the office 108a: Jacky, Laura, Beni, Tobi, Johannes and Manuel - give yourself a hand. Furthermore, this research made use of *ctools*, a community-developed analysis package for Imaging Air Cherenkov Telescope data. *ctools* is based on *GammaLib*, a community-developed toolbox for the high-level analysis of astronomical gamma-ray data.

I cannot be thankful enough to stay here, having the Master's Thesis in hand and be able to do more research in the next few years. All this would not be possible without one great strength, this strength comes from my Family. A special thanks goes to all of you!

Eidesstattliche Erklärung

Ich erkläre hiermit, dass ich die vorliegende Arbeit selbstständig angefertigt habe. Die aus fremden Quellen direkt oder indirekt übernommenen Gedanken sind als solche kenntlich gemacht. Die Arbeit wurde bisher in gleicher oder ähnlicher Form keiner anderen Prüfungsbehörde vorgelegt und auch noch nicht veröffentlicht.

Ort, Datum Unterschrift